Microseismic Constraints on the State of the North Anatolian Fault Thirteen Years after the 1999 M7.4 Izmit Earthquake

Eric Beaucé[1,3], Robert D. van der Hilst[1], Michel Campillo[2,1]

[1]Department of Earth, Atmospheric, and Planetary Sciences, Massachusetts Institute of Technology, USA
[2]Institut des Sciences de la Terre, Université Grenoble Alpes, France
[3]Lamont-Doherty Earth Observatory, Columbia University, NY, USA

Key Points:

- Detailed spatio-temporal analysis of the microseismicity in the western North Anatolian Fault Zone (NAFZ).
- Fault characterization with microearthquake statistical properties: b-value and temporal clustering.
- Interpretation of the role of different tectonic structures in accommodating motion along the NAF.

Corresponding author: Eric Beaucé, `ebeauce@ldeo.columbia.edu`

Abstract

The 17 August 1999 M_w7.4 Izmit earthquake ruptured the western section of the North Anatolian Fault (NAF) and strongly altered the fault zone properties and stress field. Consequences of the co- and post-seismic stress changes were seen in the spatio-temporal evolution of the seismicity and in the surface slip rates. Thirteen years after the Izmit earthquake, in 2012, the dense seismic array DANA was deployed for 1.5 years. We built a new catalog of microseismicity (M < 2) by applying our automatized detection and location method to the DANA data set. Our method consists of first backprojecting the seismic wavefield onto a grid of theoretical sources and then using the detected earthquakes to refine the catalog with template matching. Locations were determined with a deep neural network phase picker, an earthquake relocator, and the double-difference method. We analyzed the statistical properties of the catalog by computing the Gutenberg-Richter b-value and by quantifying the amount of temporal clustering in groups of nearby earthquakes. Our study reveals spatial patterns of seismicity that are both different to the pre- and the early post-Izmit phases. The microseismicity mainly occurs off the main fault. The statistical analysis suggests that while some of the seismicity is correlated with the low coseismic displacement, time clustered seismicity in the step-over area of Lake Sapanca indicates a previously unobserved complex dynamics. We discuss the behavior of the Lake Sapanca step-over in terms of fault structures and mechanical properties and its role in accommodating deformation along the NAF.

Plain Language Summary

On 17 August 1999, a large M7.4 earthquake struck near the city of Izmit, in western Turkey, and caused important human and material losses. The earthquake resulted from the large and sudden displacement of crustal blocks along the North Anatolian Fault (NAF). Transient changes in the crustal and fault properties are commonly observed following such large events. In this study, we analyzed the statistical properties of microearthquakes, that is, of small earthquakes (M < 2) typically too small to affect the surrounding population, to gain knowledge about the state of the NAF more than a decade after the Izmit earthquake. First, we addressed the challenge of locating microearthquakes, in space and time, by applying our automatic earthquake detection and location algorithm. Then, the statistical analysis allowed us to characterize physical properties of the NAF and, thus, to identify the prominent role of a complex section of the fault, around Lake Sapanca, in accommodating the slow deformation due to tectonic forces in the early phase following a large earthquake.

1 Introduction

The North Anatolian Fault (NAF) is a 1,500 km long strike-slip fault that marks the boundary between the Anatolian plate in the south and the Eurasian plate in the north (Figure 1A). The fault slips, overall, in a right-lateral manner to accommodate the westward motion of Anatolia with respect to Eurasia due to the combination of the subduction along the Hellenic trench and the Cyprus trench in the southwest and the south and the collision with Arabia in the southeast (Le Pichon & Angelier, 1979; McClusky et al., 2000; Reilinger et al., 2006). Near the Gulf of Izmit, in western Turkey, the NAF splits into a northern strand and a southern strand. These two strands bound the Almacik mountains in the east and the Armutlu block in the west, and separate the Istanbul Zone in the north from the Sakarya Terrane in the south, which are the remains of the passive margin of the Intra-Pontide Ocean (see Figure 1B, *e.g.* Akbayram et al., 2013). Most of the deformation is accommodated on the northern strand (*e.g.* Meade et al., 2002; Reilinger et al., 2006).

The 17 August 1999 M7.4 Izmit earthquake and the 12 November 1999 Düzce M7.2 earthquake are the most recent (as of the time of writing) events of a series of westward migrating M>7 earthquakes that ruptured almost entirely the North Anatolian Fault (*e.g.* Toksöz et al., 1979; Stein et al., 1997). The Izmit earthquake nucleated near the Izmit Bay, propagated bilaterally and broke a 150 km-long, almost vertical section of the fault made of four segments along the northern strand (Toksoz et al., 1999; Barka et al., 2002). To the east, the rupture propagated at super-shear speeds (Bouchon et al., 2001, 2011) and broke the Izmit-Sapanca, the Sapanca-Akyazi and the Karadere segments (*cf.* names on Figure 1B). To the west, the rupture propagated along the Gölcük segment and stopped on the Yalova segment (Langridge et al., 2002), increasing the risk of major failure further west beneath the Marmara Sea (Parsons et al., 2000). The Düzce earthquake nucleated near the eastern termination of the Izmit earthquake, likely due to increased Coulomb stress (Parsons et al., 2000; Utkucu et al., 2003). The co- and post-seismic stress changes and the transient changes of the fault's mechanical properties caused by the Izmit earthquake affected the local seismicity patterns and the focal mechanisms of microearthquakes (*e.g.* Bohnhoff et al., 2006; Pınar et al., 2010; Ickrath et al., 2015). GPS and interferometric synthetic aperture radar (InSAR) observations suggest that fast and rapidly decaying deep afterslip occurred in the middle-to-lower crust in the months following the Izmit-Düzce earthquake sequence (*e.g.* Reilinger et al., 2000; Bürgmann et al., 2002), then relayed by slower post-seismic slip at depth (Ergintav et al., 2009; Hearn et al., 2009). Patterns of surface displacement also suggest the existence of shallow creep along the Izmit-Sapanca and the Sapanca-Akyazi segments (*e.g.* Çakir et al., 2012; Hussain et al., 2016). Transient creep episodes have been identified more than a decade after the Izmit earthquake (Aslan et al., 2019).

Despite the overall good understanding of the east-west motion along the western NAF, smaller scale, north-south extension at some locations remains enigmatic. Co- and post-seismic slip on vertical fault segments seems unable to reproduce the patterns of north-south extension observed in geodetic data (*e.g.* Ergintav et al., 2009; Hearn et al., 2009). Even though refining the geometry of the main fault segments of the NAF helps explain the observations (*e.g.* slightly north dipping faults, Cakir et al., 2003), models of the post- and inter-seismic deformation along the NAF would benefit from taking into account secondary structures, such as the faults in step-overs. Microseismicity ($M < 2$) provides information at small length scales at seismogenic depths and thus is complimentary to geodetic data in building a better understanding of the NAF.

The dense seismic array DANA (Dense Array for North Anatolia DANA , 2012, see Figure 1C) was deployed around the rupture trace of the 1999-08-17 Izmit earthquake, it operated about thirteen years later from early May 2012 to late September 2013. These data enabled multiple studies that improved our understanding of the complex structures and seismicity patterns in the region (*e.g.* Poyraz et al., 2015; Kahraman et al., 2015; Papaleo et al., 2018; Taylor et al., 2019). Here, we study microearthquakes in order to improve our understanding of the state of the North Anatolian Fault more than a decade after the 1999 M7.4 Izmit earthquake. First, we describe briefly our automated earthquake detection and location method (Section 2), and then present the earthquake catalog (Section 3) and a statistical analysis of collective properties of earthquakes (Section 4). These observations allow a characterization of the physical environment in which seismicity takes place. We interpret and discuss our results to clarify the structural control on the post- and inter-seismic dynamics of NAF (Section 5).

2 Earthquake Detection and Location

2.1 Data

The continuous seismic data were recorded by broadband stations from the temporary array DANA (70 stations) and the permanent network KOERI (9 stations, see the locations in Figure 1, and the Data and Resources section). The time period covered by this study is set by the duration of the DANA experiment: 2012-05-04 to 2013-09-20. Sampling rates are 50 Hz for most stations and 100 Hz for a few ones. We band-

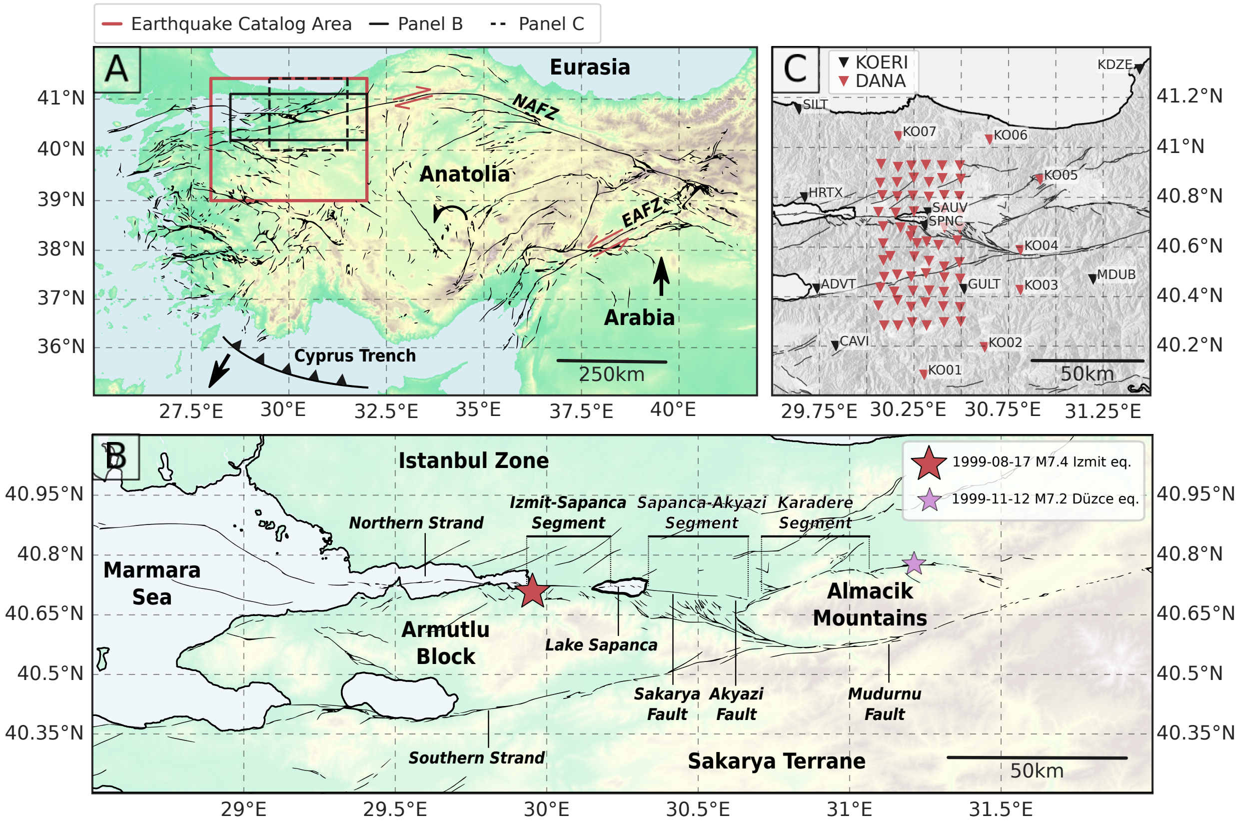

Figure 1. **A:** Large scale view of the North Anatolian Fault Zone. Abbreviations: NAFZ - North Anatolian Fault Zone, EAFZ - East Anatolian Fault Zone. The red arrows indicate the direction of coseismic motion. Our study region is located at the western end of the North Anatolian Fault (NAF). **B:** Magnified view of the fault zone in our study region. Larger font names are the main geologic units: Istanbul Zone, Armutlu Block, Almacik Mountains and Sakarya Terrane. The smaller font, italic names are segments and faults of the NAF: the Izmit-Sapanca segment, the Sapanca lake step-over, the Sapanca-Akyazi segment (which together constitute the northern strand), the Karadere segment and the southern strand (names following Barka et al., 2002). The Sapanca-Akyazi segment is made of the Sakarya fault and the Akyazi fault. The flat area around the Akyazi fault is referred to as the Akyazi plain. Both Lake Sapanca and the Akyazi plain are pull-apart basins. The large red star indicates the epicenter of the M_w7.4 Izmit earthquake, and the small purple star indicates the epicenter of the M_w7.2 Düzce earthquake. **C:** The seismic stations used in this study are from the temporary experiment DANA (70 stations, red triangles; DANA , 2012) and the permanent network (9 stations, black triangles; Kandilli Observatory And Earthquake Research Institute, Boğaziçi University, 1971). Each column of the DANA array is indexed by a letter and each row is indexed by a number (DA01, DA02, ..., DB01, ...).

pass filtered the data between 2 Hz and 12 Hz to eliminate low frequency noise and to allow us to downsample the time series to 25 Hz in order to make the computation less intensive. Useful microearthquake signal can also be found between 1 Hz and 2 Hz, but that frequency band is strongly contaminated by anthropogenic noise at some stations.

2.2 Method

We analyzed the 2012-05-04/2013-09-20 time period with a fully automatized earthquake detection and location method. The workflow, summarized in Figure 2, consists of three stages:

1. Backprojection: The energy of the seismic wavefield is continuously backprojected onto a 3D grid of potential sources to detect coherent (earthquake) sources.
2. Relocation: The P- and S-wave first arrivals of the previously detected events are identified with the automatic phase picker PhaseNet (Zhu & Beroza, 2019), and the picks are used in the NonLinLoc earthquake location software (Lomax et al., 2000, 2009).
3. Template matching: The successfully relocated earthquakes are used as template earthquakes in a matched-filter search to detect other, smaller earthquakes in the same region using the Fast Matched Filter software (Beaucé et al., 2018).

The detection method is discussed at length in Beaucé et al. (2019), but the relocation is now fully automated and includes PhaseNet and NonLinLoc. We summarize the methodology in this section.

We continuously backprojected the energy of the seismic wavefield recorded at the array of seismic stations onto a 3D grid of potential sources beneath the study region, searching for the space-time locations of coherent sources. Backprojection is now a widely used earthquake detection and source imaging method (*e.g.* Ishii et al., 2005; Walker et al., 2005; Honda & Aoi, 2009; W. Frank & Shapiro, 2014). We computed the composite network response (CNR):

$$\mathrm{CNR}(t) = \max_k \left\{ \mathrm{NR}_k(t) \right\}; \qquad \mathrm{NR}_k(t) = \sum_{s,c} \mathrm{env}\left(u_{s,c}(t + \tau_{s,c}^{(k)}) \right). \tag{1}$$

In this equation, t is the detection time and $\mathrm{NR}_k(t)$ is the network response for source location indexed by k at time t. $\mathrm{NR}_k(t)$ is the sum of the envelopes (the modulus of the analytical signal) of the seismograms $u_{s,c}$ shifted in time by the moveout $\tau_{s,c}^{(k)}$ on station s and component c. The moveouts were computed using the ray-tracing software Pykonal (White et al., 2020) in the 1D velocity model from Karabulut et al. (2011) (see Table S1). We note that the use of a 1D velocity model in this region can introduce significant errors in the earthquake locations because of the strong lateral velocity variations, in particular across the two strands of the NAF (*e.g.* Karahan et al., 2001; Kahraman et al., 2015; Papaleo et al., 2018). This velocity model produced a visually satisfying agreement between earthquake epicenters and fault surface traces, and allowed consistency with a previous study on the same data set (Poyraz et al., 2015).

All the events detected through the CNR were processed with the deep neural network PhaseNet (Zhu & Beroza, 2019) to automatically pick the P- and S-wave first arrivals. These picks were then used by the location software NonLinLoc (Lomax et al., 2000, 2009) to get the earthquake locations and their uncertainties. In theory, three differential S-to-P times are sufficient to locate an earthquake in an homogeneous earth. However, we required at least four P- and S-wave picks and a total minimum of 15 picks to relocate an event and improve chances of meaningful location. Some events could not be successfully relocated with NonLinLoc (*e.g.* noisy picks, multiple sources recorded at the same time) and were discarded. More information about the input parameters used by PhaseNet and NonLinLoc can be found in Supplementary Material (Section1).

Successfully relocated events were used in a matched-filter search to detect new, smaller magnitude earthquakes. Template matching is a powerful method for detecting low signal-to-noise ratio (SNR) events given prior knowledge of the target seismicity (*e.g.* Gibbons & Ringdal, 2006; Shelly et al., 2007; Ross et al., 2019). It consists in searching for all earthquakes with similar waveforms and moveouts to a known earthquake, that is, earthquakes sharing a similar location and focal mechanism. The similarity is measured by the network-averaged correlation coefficient (CC) between the template wave-

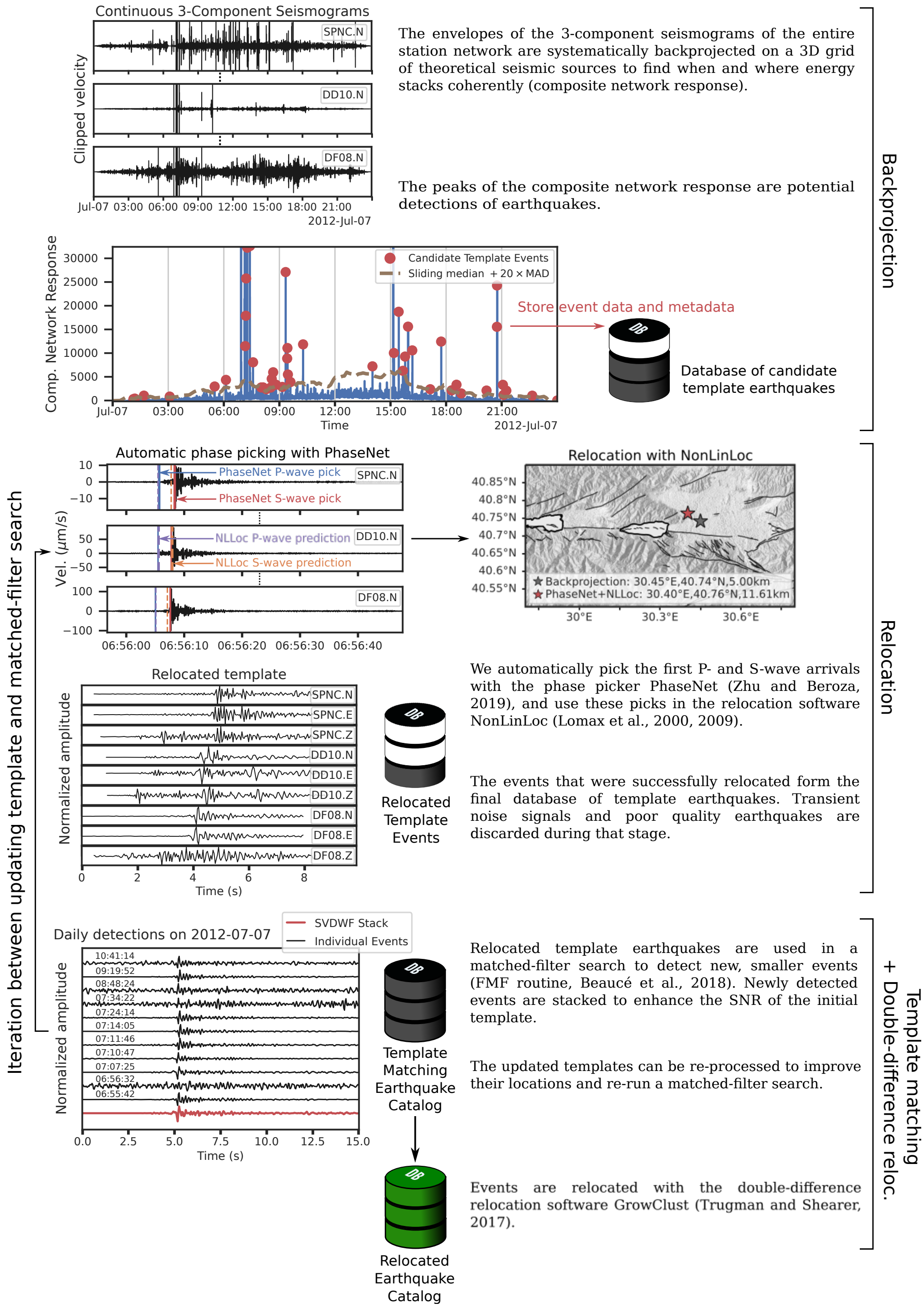

Figure 2. Summary flowchart of the earthquake detection and location method. For clarity, only a subset of stations are shown in the above panels, but all the analysis is carried on the 79 stations together. Template matching is performed on the 10 stations closest to the source and the detection threshold is set to 8×RMS of the correlation coefficients in a 30-minute sliding window. See Data and Resources for code availability.

forms $T_{s,c}$ and the seismograms $u_{s,c}$ shifted by the template moveout $\tau_{s,c}$:

$$\mathrm{CC}(t) = \sum_{s,c} w_{s,c} \sum_{n=1}^{N} \frac{T_{s,c}(t_n) u_{s,c}(t + t_n + \tau_{s,c})}{\sqrt{\sum_{n=1}^{N} T_{s,c}^2(t_n) \sum_{n=1}^{N} u_{s,c}^2(t + t_n + \tau_{s,c})}}, \tag{2}$$

where $w_{s,c}$ is the weight attributed to station s, component c, and N is the length of the template waveforms. We ran the matched-filter search on multiple nodes of a super-computer equipped with Graphic Processing Units (GPUs) using the template matching software Fast Matched Filter (Beaucé et al., 2018). We used a template length of 8 seconds and a detection threshold of 8 times the root mean square (RMS) of the CC time series in a 30-minute sliding window ($8{\times}\mathrm{RMS}\{\mathrm{CC}(t)\}$). The 8 s template duration is adequate given the signal duration of small magnitude earthquakes at $\sim$ 10-50 km source-receiver distances. The $8{\times}$RMS threshold is in the conservative range of commonly used threshold in template matching studies (*e.g.* Shelly et al., 2007; Ross et al., 2019).

After a matched-filter search over the whole study period, each template earthquake has detected potentially many new similar earthquakes. The similarity of the detected events can be leveraged to form higher SNR waveforms of the template earthquake by summing them. We used the Singular Value Decomposition and Wiener Filtering method (Moreau et al., 2017) for the efficient extraction of coherent signal in the recordings of similar earthquakes. The new template earthquakes with higher SNR waveforms were in turn used to refine the locations, and run another iteration of the matched-filter search. This detection/stacking/relocation workflow is commonly iterated several times in template matching studies. However, stacking the waveforms of similar earthquakes cancels out their differences at high frequencies, and thus acts as a low-pass filter that removes the short-scale information contained in the exact location of an individual event. In order to trade-off the SNR improvement with the loss of short-scale information, we iterated only once in this study.

The template matching catalog was refined by accurately determining the earthquake locations with the double-difference relative relocation method (*e.g.* Poupinet et al., 1984; Waldhauser & Ellsworth, 2000). P- and S-wave differential arrival times were computed by finding the lag times that maximize the inter-event correlation coefficients. The differential times were then processed by the relocation software GrowClust (Trugman & Shearer, 2017, additional information on parameters are given in Supplementary Material).

3 Direct Observations: Earthquake Spatio-Temporal Distribution

3.1 Regional Seismicity

Following the method described in Section 2.2, we built a database of 3,546 templates and with them detected 35,172 events. We note that the numbers of events reported here are after post-processing the template matching catalog. Neighboring templates often detect the same events, therefore we keep a single event out of all detections occurring within three seconds of each other, from templates whose uncertainty ellipsoids are separated by less than 5 km, and with average waveform similarity greater than 0.33. These thresholds were chosen based on physical considerations (the time threshold 3 sec assumes location errors of up to 10-15 km, the space threshold 5 km accounts for coherency of waves at 2 Hz, etc) and empirically by inspecting the output catalog for duplicated events. Figure 3 shows the locations of the 3,155 template earthquakes that are shallower than 20 km and have horizontal uncertainties less than 15 km, as well as the cumulative detection count per template over the whole study period. The majority of earthquakes occurred outside the station array and not in the NAFZ itself (see Figure 3B). We purposely present an earthquake catalog for this region that extends far beyond the NAFZ to provide a comprehensive description of the earthquake signals found in the data set. We found that most of the 1,970 events detected with templates deeper than 20 km originated far outside the study region, in particular in the Hellenic and Cyprus subduction

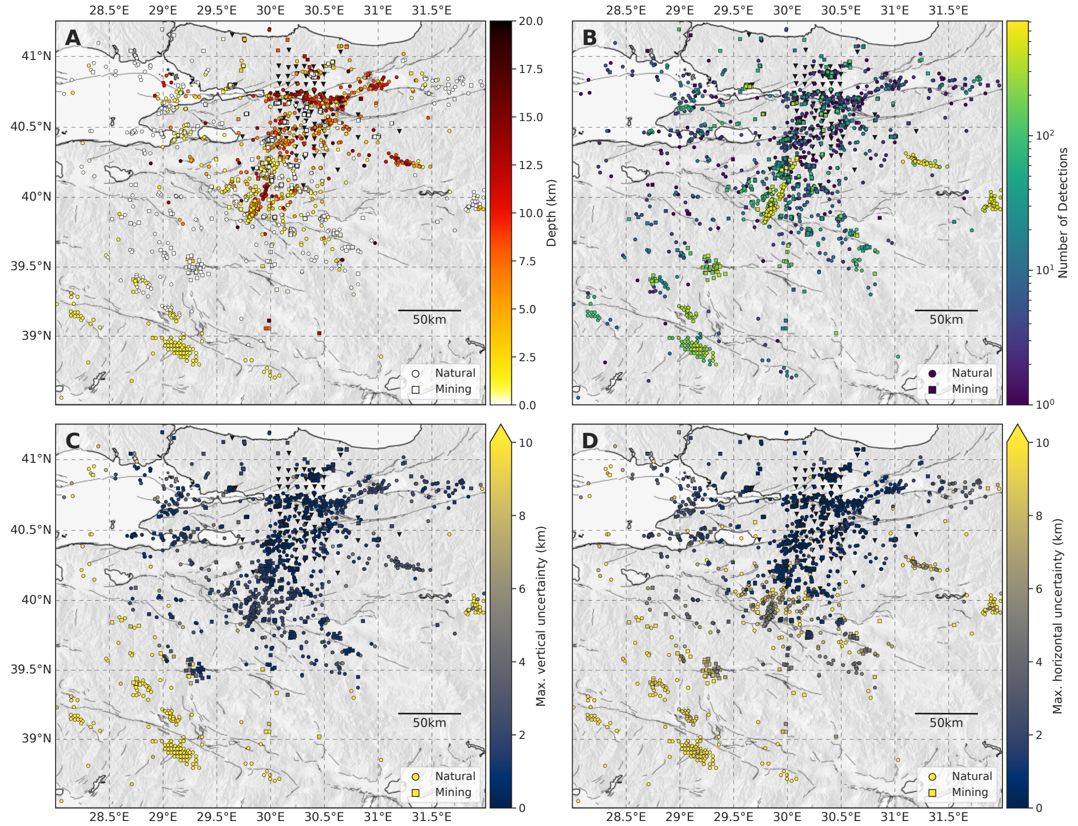

Figure 3. Map view of the locations of the template earthquakes detected and used in this study. Only templates with maximum horizontal uncertainty less than 15 km and depth less than 20 km are shown (total of 3,320 templates). Filled dots are for natural earthquakes (1,471 templates), and squares are for mining-related events (1,849 templates; see text for details about identifying templates as mining templates). **A:** Event depths. **B:** Cumulative number of event detections per template. Most of the detected earthquakes actually originate from outside the North Anatolian Fault Zone. **C:** Maximum vertical uncertainty, *i.e.* depth range spanned by the projection of the uncertainty ellipse onto a vertical plane. **D:** Maximum horizontal uncertainty, *i.e.* length of the major semi-axis of the projection of the uncertainty ellipse onto the horizontal plane.

zones in the southwest and south of the study region, respectively. Therefore, we discarded these deeper templates for any further analysis. We present the spatio-temporal distribution of the seismicity in Figure 4. The seismic activity of the region is stronger at the beginning of the study period, when we observe two sequences of slowly decaying activity due to aftershocks below 39°N and around 40°N. The southernmost earthquake sequence is part of the aftershock activity of the M5.1 2012-05-03 39.18°N/29.10°E/5.4 km earthquake (just before the deployment of DANA), but the origin of the 40°N sequence is unclear (we did not find any mainshock in the Kandilli catalog, see Data and Resources). Furthermore, we found that about half of the detected seismicity was due to mining activity.

Template matching lends itself particularly well to identifying sources of mining-related earthquakes. We identified these by analyzing the distribution of detection times within the day. Templates that detected more than 80% of events between 6am and 6pm were categorized as mining-related templates (see Figure S1 in Supplementary), since

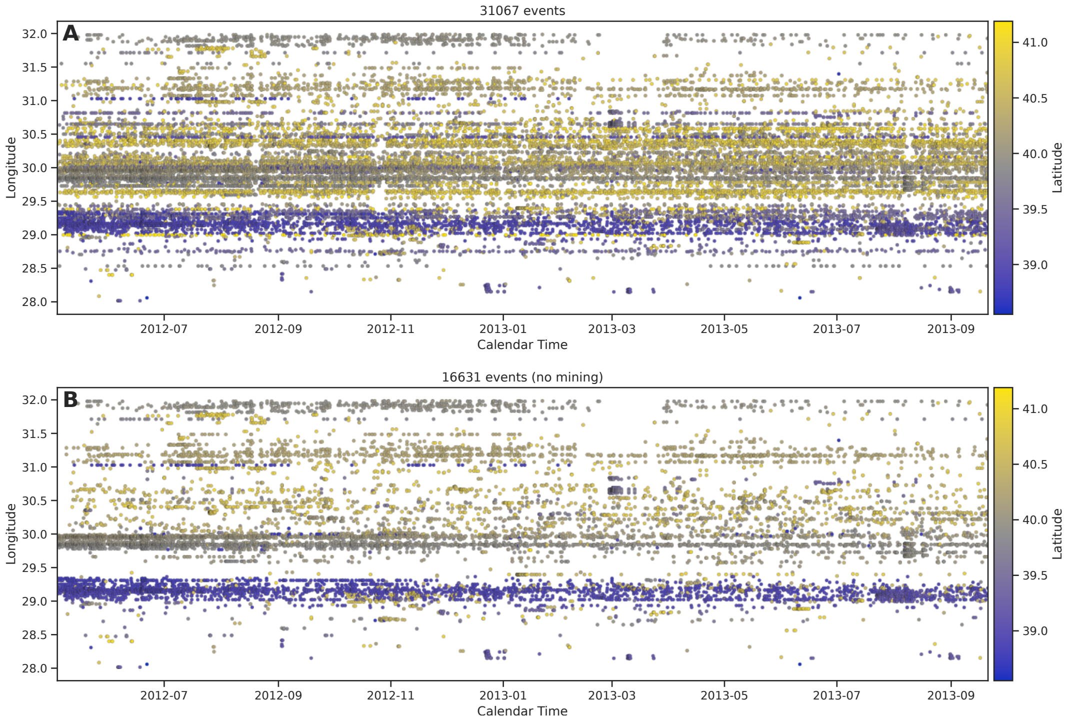

Figure 4. Spatio-temporal distribution of the earthquake activity in the study region. The longitude of each event is shown against its origin time, and the color codes the latitude. **A:** We detected 31,061 events with the 3,155 template earthquakes presented in Figure 3 from 2012-05-04 to 2013-09-20. **B:** The templates due to natural seismicity detected 16,631 earthquakes. The seismic activity taking place on the NAF (latitudes 40.40°N-40.80°N) represents a small amount of the total seismicity ($\sim$ 2,000 events).

we do not expect natural seismicity to occur within preferred times. When removing the mining-related templates, we were left with 16,631 events (*cf.* Figure 4B). The locations identified as mining-induced activity are indicated by squares in Figure 3. Both the locations and the proportion of activity ($\sim$ 50% of the total activity) are consistent with the hand-picked earthquake catalog in Poyraz et al. (2015).

Our earthquake catalog and detection/location codes are available online (see Data and Resources, and see Supplementary Material for additional information about the structure of the catalog file). This analysis of the regional seismicity shows that most of the detected seismic activity occurred outside the North Anatolian Fault Zone, which may be a feature of this section of the NAF being early in the earthquake cycle (Ben-Zion & Zaliapin, 2020). In the following, we focus on the template earthquakes located in the vicinity of the NAF.

3.2 Seismicity of the North Anatolian Fault Zone

Figure 5 shows the locations of the template earthquakes in the fault zone, as well as the 2,141 earthquakes relocated with the double-difference method (see Section 2.2). The median horizontal and vertical errors on relative locations are 73 m and 91 m, respectively, meaning that they can reliably be interpreted. Earthquake hypocenters reveal a complex network of faults, with much of the seismicity occurring on secondary faults rather than on the NAF itself. We divided the fault zone into nine subregions (*cf.* Figure 5A) whose names we will keep referring to in this manuscript. These are organized into four along-strike sections: Izmit-Sapanca, fault-parallel Sapanca-Akyazi, Karadere, and the entire southern strand, and six fault-perpendicular sections: Lake Sapanca west and east, fault perpendicular Sapanca-Akyazi, Akyazi, and the southern strand west and east. The northern strand is overall more active than the southern strand, and the Sapanca-Akyazi segment hosts the densest activity. In particular, both terminations of the segment, the eastern side of Lake Sapanca and the area around the Akyazi fault, host rich seismicity. The Akyazi region features the deepest seismicity in the vicinity of the NAF (down to 20 km). The group of earthquakes located at the northermost of the Sapanca-Akyazi region (Figure 5A-B) are part of the 2012-07-07 $M_L 4.1$ Serdivan earthquake sequence. Most of the seismicity along the southern strand occur in areas where surface fault traces indicate more complexity. Note that the relocated seismicity tends to be distributed in patches, which is partly due to the detection method. Indeed, template matching tends to detect groups of colocated earthquakes, whereas small events located in between template earthquakes may remain undetected.

The fault parallel and fault perpendicular cross-sections in Figure 5C show the events' depth distribution. The seismicity is enhanced in the lower half of the seismogenic zone. Along the northern strand, most earthquakes are located between 7 km and 15 km, and even deeper than 15 km around the Akyazi fault. The seismogenic zone in the south seems to be shallower as, there, most earthquakes are in the 5-10 km depth interval. The main exception to that depth distribution are the earthquakes on the western side of Lake Sapanca, with hypocenters clustered around 5 km depth. The Lake Sapanca W. fault perpendicular cross-section (see Figure 5C) shows that this shallow seismicity seems restricted to the southern side of the fault, namely the Armutlu Bloc.

The map views and cross-sections in Figure 5 suggest a narrower deformation zone in the north where seismicity is mostly distributed within 5-10 km of the main fault trace, whereas we observe a wider deformation zone along the southern strand with seismicity distributed within 15-20 km of the fault trace. We emphasize that the detected microseismicity illuminates the deformation zone associated with the NAF rather than the fault itself. The Sapanca-Akyazi and Akyazi fault perpendicular cross-sections could indicate a north dipping deformation zone, although these mostly show almost horizontally aligned earthquakes. Under the assumption that the deformation zone does dip towards the north, we approximately measure a 60° dip angle in the middle of the Sapanca-Akyazi segment, and 85° near the Akyazi fault. Identifying a global dip direction of the deformation zone along the southern strand is equally ambiguous. In the east, one could either identify slightly south dipping structures ($\sim 85°$) or more strongly north dipping structures ($\sim 70°$).

4 Indirect Observations: Gutenberg-Richter b-value and Temporal Clustering

4.1 Frequency-Magnitude Earthquake Distribution

The frequency-magnitude distribution of earthquakes typically follows the Gutenberg-Richter law (Gutenberg & Richter, 1941), which states that the number of earthquakes exceeding a given magnitude is described by a power-law:

$$\log N(M) = a - bM. \tag{3}$$

In Equation (3), $N(M)$ is the number of earthquakes exceeding magnitude M, the a-value depends on the total number of observed events, and the b-value controls how frequent larger earthquakes are (typically $b \approx 1$). We estimated the b-value with the maximum likelihood technique (Aki, 1965):

$$b = \frac{1}{\ln(10)\left(\bar{M} - M_c\right)}. \tag{4}$$

Equation (4) is derived for continuous magnitudes M (no bias from binned magnitudes). M_c is the magnitude of completeness, *i.e.* the magnitude above which all events are de-

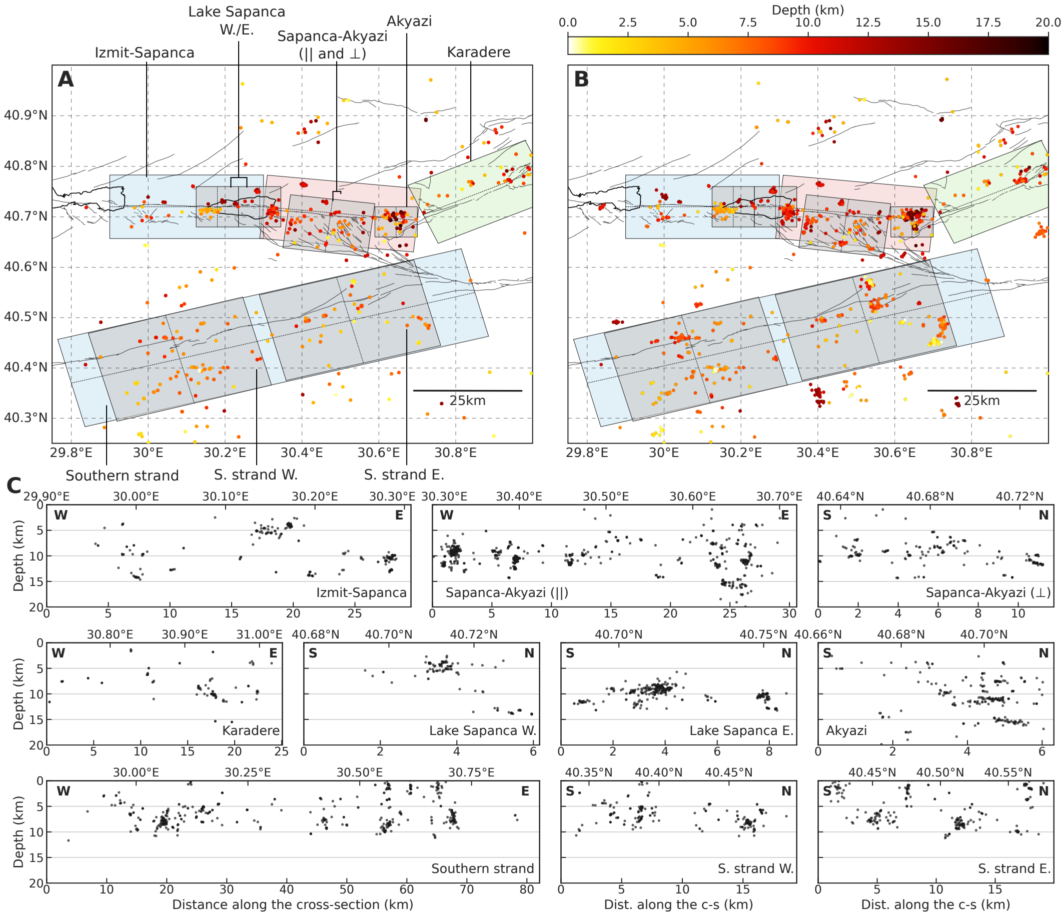

Figure 5. Earthquakes in the North Anatolian Fault Zone. **A:** Locations of the template earthquakes with color coded depths. We define nine subregions along the different segments of the fault. Only in this figure the Sapanca-Akyazi region is subdivided into a fault parallel and a fault perpendicular sections. The thin black dotted lines inside each colored box define either fault parallel or fault perpendicular cross-sections (see bottom panels, C). The color shading of each box is only to help distinguish between them. **B:** Earthquake hypocenters successfully relocated with the double-difference method and color coded by depth. Events for which relocation was not successful were attributed the template location. **C:** Depth cross-sections of the different areas introduced above. The earthquake locations contained in the boxes are projected onto the boxes' central axis. The bottom x-axes are distances along the cross-section axes in kilometers, and the top x-axes are the geographic coordinates relevant to each cross-section (either longitude or latitude). Note that the x scales across different cross-sections do not match.

tected. We estimated M_c with the maximum curvature technique (*e.g.* Wiemer & Katsumata, 1999), which simply consists in taking the most populated magnitude bin of the frequency-magnitude histogram as the magnitude of completeness.

Earthquake magnitudes were computed from log ratios of peak amplitudes between all events and co-located reference events for which a moment magnitude could be determined (see Figure S2 and Section S1.7 for more information). We estimated b and M_c for each template by taking all events detected with templates located within a 5 km-radius of the given template. For robust estimation, we required at least 30 earthquakes with valid magnitude estimates to compute the b-value, and therefore most templates do not have a b-value estimate. Results are presented in Figure 6. Of most interest to this study, we see that earthquakes at the eastern side of Lake Sapanca exhibit high b-values ($b \approx 1.2$), whereas earthquakes near the Akyazi fault show low b-values ($b \approx 0.8$). We note that visual checking of the frequency-magnitude distributions showed that, in general, they follow the Gutenberg-Richter law well, except for the Serdivan earthquakes where a peak around $M_L \approx 2.5$ can be observed.

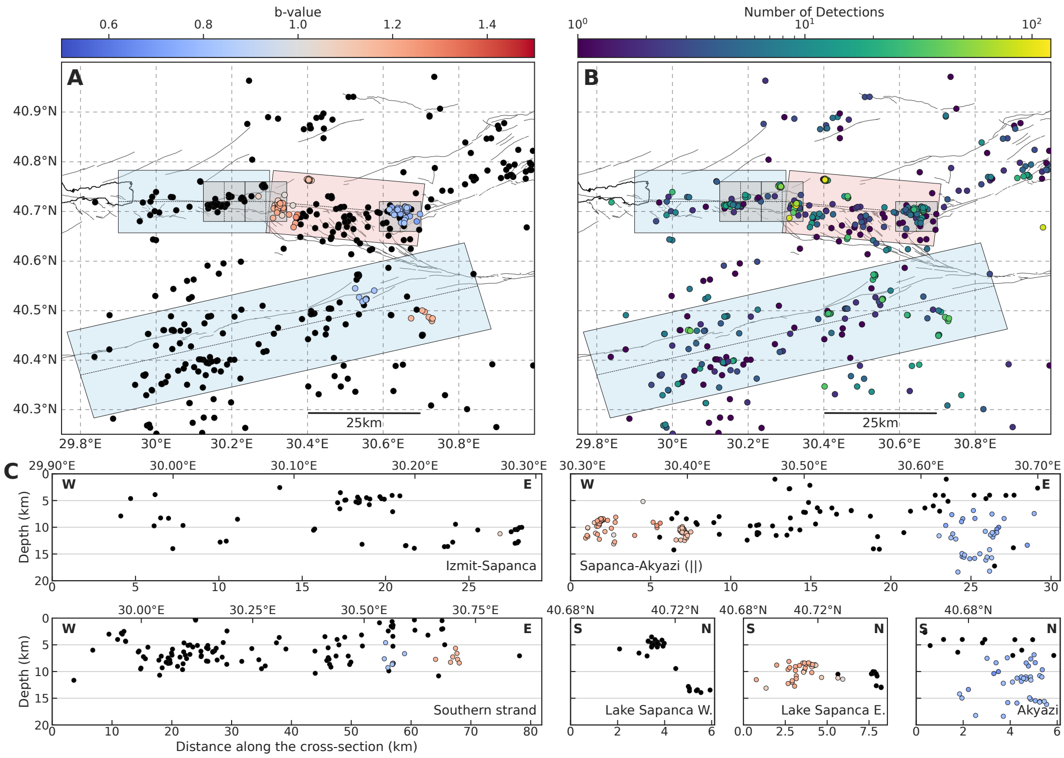

Figure 6. **A:** Map view of template earthquakes with color coded Gutenberg-Richter b-value. **B:** Map view of template earthquakes with color coded cumulative number of detections. In both top panels, the shaded areas refer to the regions introduced in Figure 5. **C:** Template earthquakes with color coded b-value on fault parallel and fault perpendicular cross-sections. Hypocenters are projected along the dotted axes shown on the map view.

4.2 Earthquake Temporal Clustering

In this manuscript, we refer to temporal clustering as the property of earthquake sequences in which events influence the timings (advance or delay) of future earthquakes, that is, the non-randomness of earthquake sequences (*e.g.* Gardner & Knopoff, 1974; Marsan & Lengline, 2008). We stress that a transient increase in seismicity does not necessarily imply a time clustered earthquake sequence (see Figure S4), as it could reflect a transient increase in the background (random) seismicity due to some transient change in the background stressing (*e.g.* fluid injection at a well).

Figure 7 shows the temporal evolution of the earthquake recurrence times. The recurrence time is the time interval between two consecutive co-located earthquakes. In practice, recurrence times are computed as the time intervals between consecutive events detected by a same template. The most striking feature of Figure 7 is the organization of some earthquake sequences into bursts of seismicity with recurrence times spanning many orders of magnitude. During these special episodes, earthquakes occur at all time scales, from every day to every few seconds, which is an indication of temporal clustering (*e.g.* W. B. Frank et al., 2016; Beaucé et al., 2019). These bursts are usually associated with sequences of foreshocks-mainshock-aftershocks, although in general earthquake sequences can have no clear mainshock (that is, an event of magnitude larger than all other events of the sequence) can still exhibit a strong burst-like behavior. The seismicity at the eastern end of Lake Sapanca and near Akyazi is almost exclusively organized into such sequences of burst-like seismicity, whereas the southern strand hosts much less of these burst-like episodes. Figure 7 also reports the local magnitudes (see Section 4.1). The Sapanca-Akyazi segment and its vicinity is the most active region with the largest magnitude events observed during the study period. Among the nine $M_L \gtrsim 3$ natural earthquakes we detected, three occurred near each other, close to the city of Serdivan, including the largest event of the study: the 2012-07-07 $M_L 4.1$ Serdivan earthquake (30.404°E/40.763°N/11.3 km). The area around the Akyazi fault also produced four $M_L > 3$ earthquakes, whereas earthquakes near Lake Sapanca did not exceed $M_L = 3$.

We quantified the strength of temporal clustering in earthquake sequences by analyzing the statistical properties of the number of earthquakes per unit time, which we refer to as the earthquake occurrence time series. It is given by:

$$e(t) = \text{Number of events} \in [t; t + \Delta t] \,, \tag{5}$$

where Δt is a user-defined time bin duration, and t is the calendar time. An example is given in Figure 8A. Burst-like sequences covering wide intervals of recurrence times are not random, unlike background seismicity (see Figure 8B,C). Namely, burst-like seismicity is clustered in time. Further analysis shows that time clustered seismicity exhibits time scale invariant characteristics. The spectrum of the earthquake occurrence $e(t)$ (as computed by Equation (5)) follows a power law of frequency ($\propto f^{-\beta}$, see Figure 8D), and the time series $e(t)$ shows a fractal organization (Figure 8E). The fractal dimension of the earthquake occurrence time series is measured by subsequently dividing the time axis into smaller and smaller time bins (varying size τ), and counting the fraction of bins x that are occupied by at least one earthquake (Smalley Jr et al., 1987; Lowen & Teich, 2005). For a certain range of time bin sizes τ, we observe:

$$x \propto \tau^{1-D}. \tag{6}$$

In Equation (6), D is the fractal dimension of the time series. The fractal dimension varies between the two end-members $D = 0$ for a point process (*e.g.* Poisson point process for the background seismicity), and $D = 1$ for a line (uninterrupted seismicity). A large fractal dimension ($D > 0.2$) characterizes cascade-like activity where past events strongly influence the timings of future events. Fractal analysis has been used in multiple studies to characterize earthquake clustering (Smalley Jr et al., 1987; Lee & Schwarcz, 1995; Beaucé et al., 2019). Note that periodic seismicity does not follow a fractal behavior and cannot be characterized by this method.

In general, the shape of the spectrum (Figure 8D) is much more complex than that of the fractal statistics $x \propto \tau^{1-D}$ (Figure 8E). Thus, estimating the fractal dimension D is more robust than estimating the spectrum power-law exponent β, therefore we chose the fractal dimension to characterize temporal clustering in the rest of this study. We also note that temporal clustering is sometimes studied with the distribution of recurrence times (*e.g.* Hainzl et al., 2006), but we found that the relatively small earthquake sequences in this study were not well suited for such analysis (the distribution cannot be accurately estimated, see, for example, Figure S3).

The above method does not explicitly deal with space. However, we applied this analysis to subsets of the earthquake catalog containing neighboring earthquakes (as described for the b-value, see Section 4.1), and thus obtained a fractal dimension for each template. The resulting analysis characterized temporal clustering as a function of space (see Figure 9). The strongest temporal clustering ($D > 0.20$) is observed on the eastern side of Lake Sapanca, beneath the so-called Rangefront trace. Other areas of strong activity, like the Serdivan earthquakes (around 30.404°E/40.763°N) and the Akyazi area,

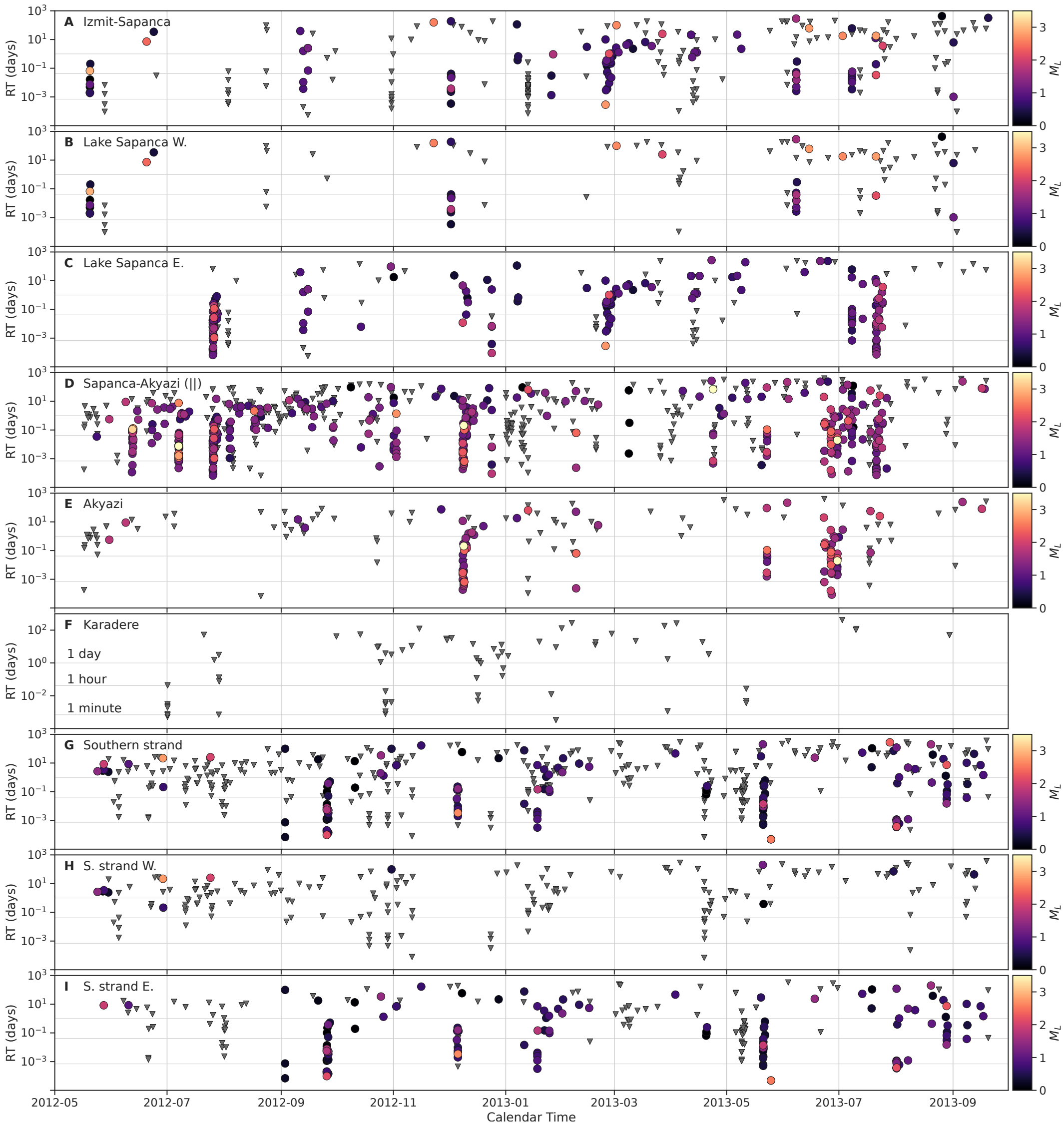

Figure 7. Time evolution of the earthquake recurrence times for different subsets of the earthquake catalog (refer to Figure 5 for the name of the areas). The recurrence time is the time between two consecutive events detected by a same template. Note that the y-axis is in log scale and that some seismic episodes span many orders of magnitude of recurrence time. These episodes are characteristic of burst-like, or cascade activity (see text). The color scale indicates the local magnitude, and inverted grey triangles are events for which no reliable estimates were obtained.

only show small-to-moderate temporal clustering ($D < 0.14$), thus confirming the outstanding character of the eastern Lake Sapanca. We note that while the temporal organization of recurrence times shown in Figure 7 indicated burst-like seismicity in all of the above mentioned areas, this quantitative analysis was necessary to distinguish between strongly and moderately time clustered sequences. A few other isolated locations exhibit strong temporal clustering, and seem to be systematically occurring near the bottom of the seismogenic zone (*cf.* Figure 9C). Comparing the cumulative number of detections per template and their fractal dimension shows that there is no trivial correla-

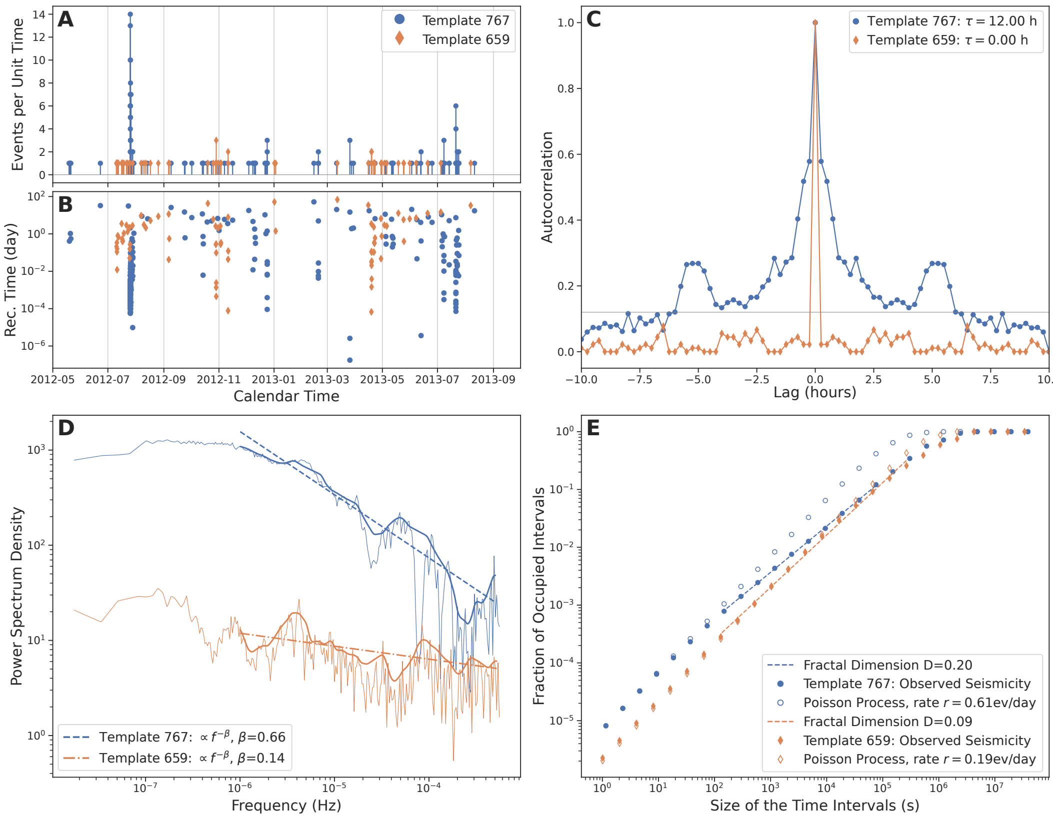

Figure 8. Quantifying the strength of temporal clustering in a strongly clustered sequence (Template 767, blue dots) and a weakly clustered sequence (Template 659, orange diamonds). **A:** Number of earthquakes per unit time (referred to as earthquake occurrence, see Equation (5)). **B:** Recurrence times vs. origin times. **C:** Autocorrelation of the earthquake occurrence time series. The horizontal black line is the arbitrary threshold used to define the correlation time τ. **D:** Power spectral density of the earthquake occurrence. The linear trend, in the log-log space, is the exponent of the power-law that indicates a scale invariant process. **E:** Fractal analysis of the earthquake occurrence (see text and Equation (6)). We measure the slope between dt_{min}=100 s and $dt_{\mathrm{max}} = 1/r$, where $r = N/T$ is the average seismic rate (number of events N divided by time span T). For reference, for each template we simulate the seismicity from a Poisson point process with average rate r. The slope of the Poisson point process gives a fractal dimension $D = 0$ (*i.e.* dimension of a point).

tion between the two (see Figure 9A vs. B). We note that we did the same fractal analysis on all templates of the study region and found another region of strong temporal clustering on the NAF, in the eastern Marmara Sea, where the 1999 Izmit earthquake arrested (see Figure S5).

5 Interpretation and Discussion

5.1 Spatial Distribution of Seismicity

We combined different earthquake catalogs to compare the 2012-2013 detected seismicity with the pre-Izmit, Izmit-Düzce, and early post-Düzce seismicity (Bulut et al., 2007; Ickrath et al., 2015; Bohnhoff et al., 2016, and see Figure 10). We note that the Izmit-Düzce earthquake catalog is more complete in the west (around the Izmit-Sapanca

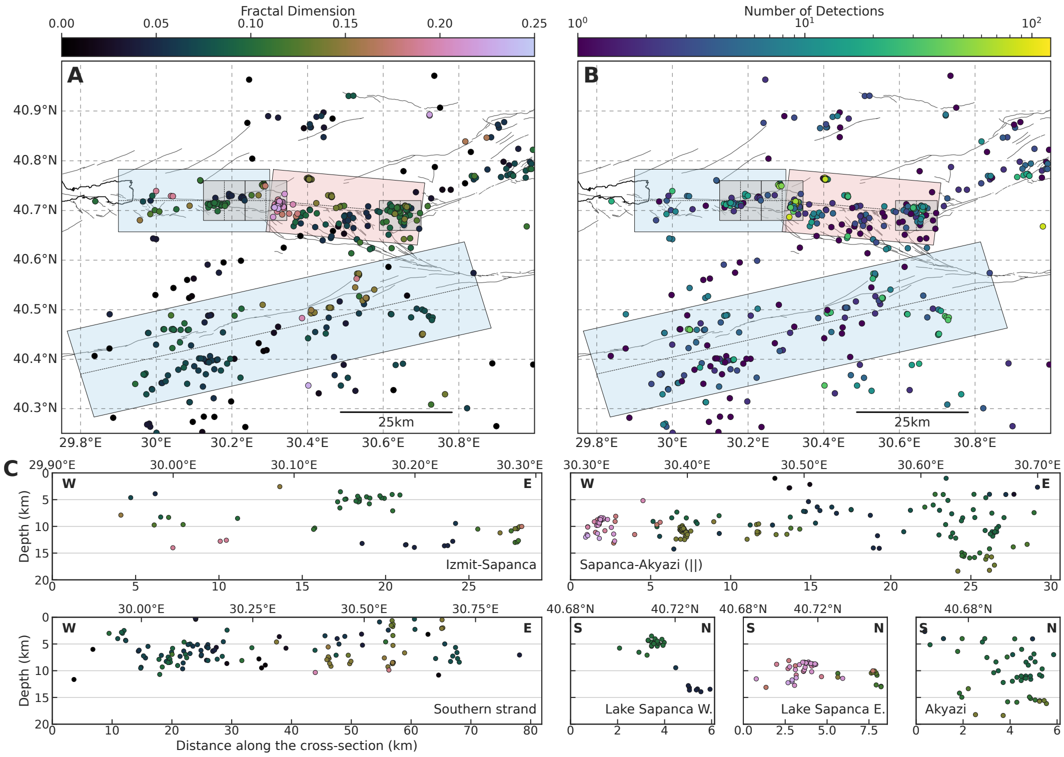

Figure 9. **A:** Map view of template earthquakes with color coded fractal dimension (*cf.* Equation (6)) showing the strength of temporal clustering. **B:** Map view of template earthquakes with color coded cumulative number of detections. In both top panels, the shaded areas refer to the regions introduced in Figure 5. **C:** Template earthquakes with color coded fractal dimension on fault parallel and fault perpendicular cross-sections. Hypocenters are projected along the dotted axes shown on the map view. High fractal dimensions mean strongly time clustered activity (*i.e.* past events strongly influence the timings of future events).

segment) than the pre-Izmit and early post-Düzce catalogs due to the higher number of stations used in this time period (see, *e.g.* Ickrath et al., 2015). It is also worth mentioning that these three catalogs show both natural and mining-related seismicity whereas we have discarded the man-made seismicity to the best of our ability (see Section 3.1).

The middle sections of the Izmit-Sapanca and Sapanca-Akyazi segments were particularly active seismically before the Izmit earthquake, and some clusters of earthquakes were observed beneath Lake Sapanca (Figure 10A). The Izmit earthquake is known to have nucleated near a swarm of seismicity that was active before the M7.4 event (Crampin et al., 1985; Lovell et al., 1987). In the three months between the Izmit earthquake and the Düzce event, the seismic activity was strongest in the area around the triple junction between the Sapanca-Akyazi segment, the Karadere segment, and the Mudurnu fault (Figure 10B). The Izmit hypocentral region remained active but, comparatively, little activity was detected near Lake Sapanca. After the Düzce earthquake, most activity along the Izmit-Sapanca and Sapanca-Akyazi terminated, and seismicity concentrated along the Karadere segment (Figure 10C). The Akyazi region, where little coseismic slip was observed (Ozalaybey et al., 2002; Bohnhoff et al., 2006, 2008), hosted a cluster of strong activity, possibly driven by the Izmit residual stresses. Note that no seismicity was detected near Lake Sapanca. About 13 years after the Izmit and Düzce earthquakes, we detected the strongest activity at the eastern side of Lake Sapanca, and near the Akyazi fault (Figure 10D). If not due to insufficient detection capability, the lack of intense seis-

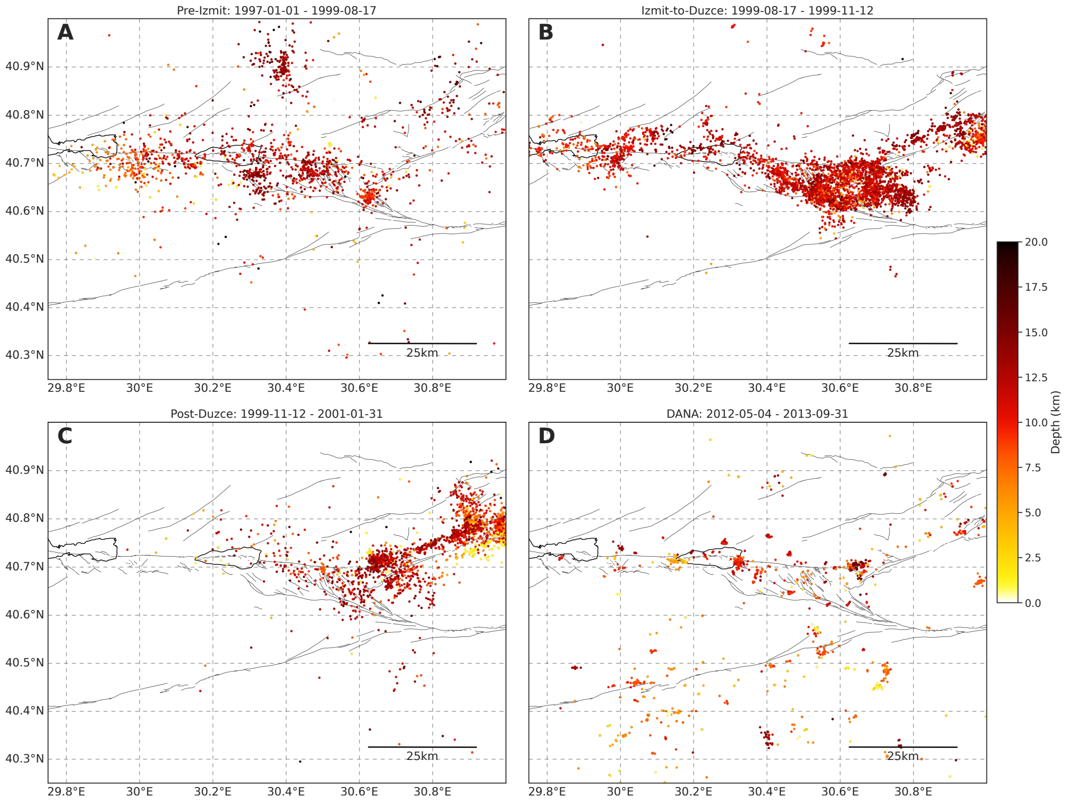

Figure 10. Comparison of the **A:** pre-Izmit, **B:** Izmit-Düzce, **C:** early post-Düzce, and **D:** late post-Düzce seismicity. The apparent shutdown of seismicity in the west between panels B and C is partly due to the removal of many stations.

micity near Lake Sapanca in the early post-Düzce period suggests that faults near Lake Sapanca did not contribute to the afterslip-driven aftershock sequence with Omori-like temporal decay (Perfettini & Avouac, 2004). Instead, the Omori law predicts a seismicity rate about four orders of magnitude lower 13 years after the mainshock (Bayrak & Öztürk, 2004). Furthermore, the 2012-2013 Lake Sapanca seismicity also appears much stronger than the pre-Izmit seismicity (Figure 10A). We can speculate that the Lake Sapanca seismicity either indicates some temporal evolution of the mechanical state of the fault zone in response to the Izmit-Džuce earthquake sequence, or that is associated with transient deformation episodes that were not observed in the year following the Düzce earthquake (*cf.* further discussion in Section 5.4). Variations in seismicity along the southern strand are harder to interpret because the lack of earthquakes in previous catalogs (see Figure 10) is partly due to the absence of stations in the past.

Except for the Karadere segment, the seismicity is taking place off the main fault on a complex network of secondary faults, similarly to the Izmit-Düzce aftershocks (*e.g.* Ozalaybey et al., 2002; Bulut et al., 2007). This feature is in stark contrast with the simplicity of the Izmit and Düzce earthquakes, which occurred on simple fault segments (Barka et al., 2002; Langridge et al., 2002). Off-fault seismicity has also been observed to be a characteristic of fault zones early in their seismic cycle (Ben-Zion & Zaliapin, 2020).

Shallow creep has been observed along the Izmit-Sapanca and the Sapanca-Akyazi segments (*e.g.* Çakir et al., 2012; Hussain et al., 2016; Aslan et al., 2019), which should drive microseismicity in the vicinity of the creeping fault sections (*e.g.* Lohman & McGuire, 2007). The depth cross-sections (Figure 5C) do not suggest the existence of sustained seismicity at shallow depths. However, the depth of the shallow creep seems hard to constrain (see, for example, the very large confidence intervals on the shallow creeping depth in Hussain et al., 2016) and may also be a fault property that evolves with time (*e.g.* Bürgmann et al., 2002). Concluding on the seismic signature of potential shallow creep based on these depth cross-sections is therefore difficult. Moreover, most of the seismicity occurs off the main fault (Figure 5B), which further complicates any interpretation of the seismicity in terms of processes happening on the main fault. However, the spatial distribution of earthquakes suggests that, at the time of the study, the base of the seismogenic zone is around 10-15 km, which is in good agreement with the estimates in Aslan et al. (2019) based on 2011-2017 geodetic data.

5.2 Gutenberg-Richter b-value

Large b-values are sometimes thought of indicating strongly heterogeneous (*e.g.* highly fractured) media (Mogi, 1962). However, laboratory experiments have shown that the b-value seemed to be controlled by the state of stress rather than the properties of the medium, specifically that b decreases with increasing differential stress (*e.g.* Scholz, 1968; Amitrano, 2003). The apparent depth dependence of the b-value of actual earthquakes (Mori & Abercrombie, 1997; Wiemer & Wyss, 1997) and the b-value difference between foreshocks and aftershocks (*e.g.* Gulia & Wiemer, 2019) support this interpretation beyond the laboratory. Furthermore, estimates of differential stresses in Earth have also shown a negative correlation with b-value (Scholz, 2015). Creeping fault sections have been reported to host high b-value seismicity (*e.g.* Amelung & King, 1997; Wiemer & Wyss, 1997), further supporting that low stress environments cause high b-value seismicity.

Our results (Figure 6) show two regions with high b-values, that is, with low background stresses: the eastern side of Lake Sapanca, and a secondary structure off the southern strand. Two regions appeared to host low b-value seismicity, that is, with high background stresses: around the Akyazi fault, and on the eastern section of the southern strand near its junction with the Mudurnu fault. These results suggest that the seismicity at the eastern side of Lake Sapanca is taking place on weak faults, explaining the low stress-drop and high b-value seismicity, where both seismic and aseismic slip could be mixed. The strong seismic activity in the Akyazi area appears to be taking place under higher stress conditions, most likely still driven by the residual stresses left by the small Izmit coseismic displacements on this section.

5.3 Temporal Clustering, Earthquake Interactions, and Fault Mechanical Properties

Strongly time clustered seismicity, as presented in Section 4.2, cannot be explained only by fluctuations of the background seismicity rate, for example due to the injection of fluids at depth. Indeed, a Poisson point process with a transient increased rate cannot reproduce the observed distribution of recurrence times and the fractal dimensions $D \gtrsim 0.20$ (*cf.* Figure S4). Temporal clustering, that is, cascading of events, emerges when different faults or sections of a fault interact (*e.g.* Burridge & Knopoff, 1967; Marsan & Lengline, 2008; Fischer & Hainzl, 2021). Earthquakes can trigger each other due to the static stress changes induced by the co- and postseismic displacements (*e.g.* King & Cocco, 2001), but also due to the dynamic stress changes induced by the elastic waves radiated by the rapid coseismic motions (*e.g.* Fan & Shearer, 2016). Furthermore, because of the stress redistribution following any slip motion (not necessarily at seismic speeds), interaction can occur between a seismogenic asperity and its creeping surroundings, an acceleration of creep (*e.g.* afterslip) resulting in an increased stressing rate on the asperity (*e.g.* Cattania, 2019; Cattania & Segall, 2021). In realistic, complex conditions where seismic and aseismic slip co-occurs on short length scales, numerical models show that both co-seismic and creep mediated stress changes are important factors controlling the clustering of earthquakes (Dublanchet et al., 2013; Cattania & Segall, 2021). The contribution of creep mediated stress transfers to temporal clustering might even be more important than static stress changes due to the breaking of asperities (Dublanchet, 2019). In fact, this means that both seismic and aseismic events can cluster in time, but that earthquake catalogs only capture the seismic signature of temporal clustering. Effectively, these interacting stress fields result in a clock advance or delay in the cycle of the earthquake sources (*e.g.* Harris et al., 1995; Gomberg et al., 1998) and thus in non-random earthquake sequences.

Figure 11 sketches different earthquake interaction scenarios explaining temporal clustering: in a locked fault Figure 11A, and with creep mediated stress transfers Figure 11B. Note that remote creep acting on a sparse asperity population (Figure 11C) would produce Poissonian seismicity (*e.g.* Lohman & McGuire, 2007). Thus, areas of strong temporal clustering (see Figure 9) indicate faults with intrinsic properties that promote interaction-driven seismicity and, consequently, fractal patterns in the earthquake occurrence. However, the long time-scale behavior of clustered seismicity may, however, be modulated by time-dependent remote forcing.

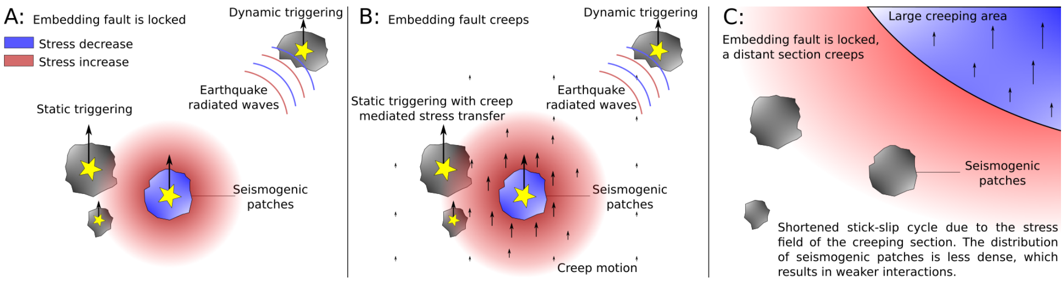

Figure 11. Sketch of different earthquake interaction scenarios. **A:** Seismogenic asperities embedded in a locked fault. **B:** Seismogenic asperities embedded in a creeping fault. In **A** and **B**, the color shows the stress change due to rupture of the seismogenic patch. The triggered ruptures occur with some delay. **C:** Seismogenic asperities embedded in a locked fault, but stressed by a remote creeping section of the fault. The asperities are not close enough to the creeping patch to strongly interact via static stress changes. The spatial configuration of asperities does not promote strong interactions.

Where rheology transitions from brittle to ductile, for example at the base of the seismogenic zone, faults are likely to host both unstable, seismic slip and stable, aseismic slip (Scholz, 1998). Indeed, seismicity near the bottom of the seismogenic zone would be expected to display temporal clustering because, there, interacting asperities are likely to be embedded in a creeping fault (*cf.* Figure 11B, Dublanchet et al., 2013). We investigated the relationship between temporal clustering and the proximity to the bottom of the seismogenic zone to elucidate the role of fault stability in our observations (*i.e.* scenario Figure 11A vs. 11B). The results, in Figure 12, indicate that, as expected, temporal clustering tends to increase in strength as we move closer to the brittle-ductile transition and that strong clustering almost always happens at the bottom of the seismogenic zone. Exceptions are at the western side of Lake Sapanca (Figure 12B) where results might be biased due to the absence of significant seismicity at depth, and along the Karadere segment (Figure 12F) where large source-receiver distances yield poor hypocentral depth resolution and thus low confidence results.

We also investigated a possible correlation between the proximity to the brittle-ductile transition and the density of seismic sources, which could as well explain the increase in temporal clustering. We took the average inter-event distance within neighboring earthquake subcatalogs as a proxy for asperity density. We note that this measure of asperity density is imperfect because a single asperity can break repeatedly. The smaller number of detected earthquakes along the southern strand might also be insufficient to

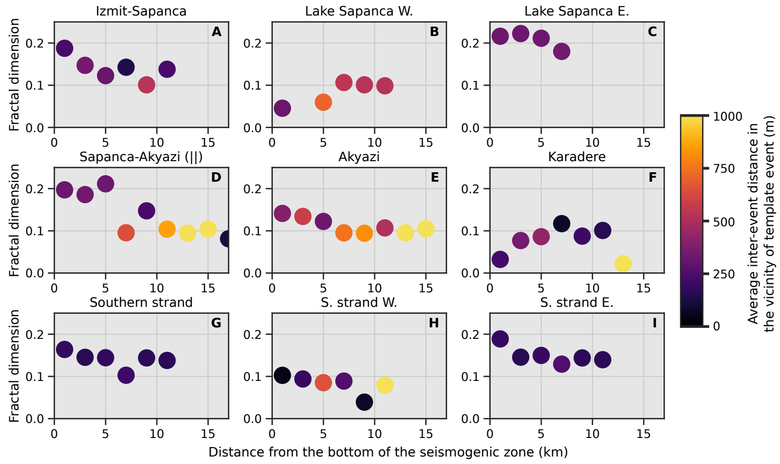

Figure 12. Clustering vs. depth vs. event density. Inside each region, templates are binned per distance from the bottom of the seismogenic zone and the fractal dimension is averaged among the 10% largest values, resulting in a "soft" maximum of each bin. The location of the bottom of the seismogenic zone is approximated by the depth of the locally deepest template. Dots are colored according to the average inter-event distance within the neighboring earthquake subcatalogs; this is a proxy for asperity density. Darker colors mean higher density. Strongest clustering tends to occur at the bottom of the seismogenic zone, *i.e.* at the transition zone between unstable (brittle) and stable (ductile) sliding.

compute a meaningful average inter-event distance. We do not observe a clear systematic increase in asperity density with decreasing distance from the bottom of the seismogenic zone, but the observational limits mentioned above prevent us from drawing definite conclusions. Figure 12 rather shows that both the proximity to the brittle-ductile transition and a large event density favor temporal clustering. Our observations therefore support that dense asperity populations along with creep mediated stress transfers do promote strong temporal clustering (*cf.* Figure 11B, Dublanchet et al., 2013). Thus, this study suggests that faults at the eastern side of Lake Sapanca work in mixed stability regimes allowing unstable (seismic) and stable (aseismic) slip.

5.4 Implications for the Lake Sapanca Step-Over

The Gutenberg-Richter b-values (see Section 5.2) and the observations of temporal clustering (see Section 5.3) point to the role of different rheological properties in producing earthquakes between the two sides of Lake Sapanca. At the western side, the shallow activated sections seem incapable of producing strongly time clustered seismicity. At the eastern side, the depth distribution and the strong temporal clustering (Figure 9C) suggest that faults are almost fully aseismic with a thin depth range where closely or co-located seismic and aseismic slip is possible. Geologic data suggest that the so-called Sapanca Complex, constituted of weak serpentinites and strong metabasites (Akbayram et al., 2013, and references therein), might reach the southeastern side of Lake Sapanca at depth where we observe the highly clustered seismicity. Such lithology is consistent with the scenario of strong asperities embedded in a weak, creeping fault.

Geodetic data show that deformation around the Lake Sapanca step-over accelerated considerably following the Izmit earthquake (Ergintav et al., 2009; Hearn et al., 2009), supporting the hypothesis that the step-over underwent significant mechanical changes during the Izmit-Düzce earthquake sequence as suggested by the history of seismicity (see Section 5.1). Previous studies have documented both the weakening of the NAF around

Lake Sapanca following the Izmit earthquake (with principal stress analyses, *e.g.* Pınar et al., 2010; Ickrath et al., 2015), and the time-dependent nature of postseismic slip distribution along the NAF (*e.g.* Bürgmann et al., 2002; Hearn et al., 2009). Thus, the activation of seismicity in the late postseismic stage might be a consequence of combined effects such as the acting of background tectonic stresses on weakened structures, and/or of the reloading due to postseismic deformation. The delayed onset of the Lake Sapanca activity with respect to the Izmit earthquake could be explained by the dynamic nature of the NAF's postseismic response.

Faults with weakly unstable sections (that is, near the stable-unstable transition) may produce transient episodes of slow slip (*e.g.* Bürgmann, 2018). The temporal distribution of earthquakes near Lake Sapanca (see Figure 7C) supports the idea of intermittent deformation with strong seismicity occurring during slow slip episodes. Since transient aseismic deformation along the Izmit-Sapanca and Sapanca-Akyazi segments have been observed (Aslan et al., 2019), we propose that such slow slip episodes may also occur on faults in the Lake Sapanca step-over and activate seismicity on the seismogenic sections. Shallow seismicity at the western side of Lake Sapanca could be due to shallow creep on the Izmit-Sapanca segment (Çakir et al., 2012; Hussain et al., 2016; Aslan et al., 2019). Intermittent deformation in the step-over may be accommodating the stressing caused by slip at depth on the main fault segments.

The postseismic response of at least two releasing step-overs of the NAF, Lake Sapanca and another one in the eastern Marmara Sea, has been shown to produce substantial north-south extension (Ergintav et al., 2009; Hearn et al., 2009). Ergintav et al. (2009) have shown that models of postseismic slip on the main fault do not account well for the north-south extension in these two step-overs, in particular after the first three years. Extending our temporal clustering analysis further along the NAF revealed that the eastern Marmara Sea was also an area hosting clustered seismicity (*cf.* Figure S5). Large earthquake location uncertainties prevented us from carrying the same detailed study but we can hypothesized that Lake Sapanca and the eastern Marmara Sea behave similarly. Thus, our study points to the important role of these two releasing step-overs in accommodating the deformation along the NAF, and, therefore, models of deformation through the earthquake cycle would probably benefit from taking into account motion in the step-overs.

6 Summary and Concluding Remarks

We processed 1.5 years of continuous data collected during the DANA experiment (May 2012 - September 2013, see Data and Resources) with an automated earthquake detection and location method (Beaucé et al., 2019, and see Section 2) and produced an earthquake catalog with 35,172 events (*cf.* Section 3). We found that about half of the detected events were induced or triggered by mining activity and that most naturally occurring earthquakes occurred outside of the North Anatolian Fault Zone itself. We focused our analysis on about 2,000 relocated earthquakes in the NAFZ and near the station array.

We analyzed the earthquake catalog to investigate collective properties of earthquakes: the b-value of the Gutenberg-Richter law (see Section 4.1), which we related to the level of background stresses driving the ruptures (*e.g.* Scholz, 1968; Amitrano, 2003; Scholz, 2015, see Section 5.2), and the strength of temporal clustering (see Section 4.2), which we interpreted in terms of interacting stress fields (King & Cocco, 2001; Dublanchet et al., 2013; Fan & Shearer, 2016, see Section 5.3). We showed that strongest temporal clustering almost systematically occurred in the brittle-ductile transition zone, emphasizing the importance of rheology in interpreting temporal clustering (*cf.* Section 5.3).

We found that the patterns of seismicity have changed durably after the Izmit-Düzce earthquake sequence even after the termination of the aftershock activity (see Section 5.1 and Figure 10). The region near the Akyazi fault, where the co-seismic displacement was noticeably low, was still one of the most active areas some thirteen years later. This seismicity indicate a low b-value ($b \approx 0.8$, *cf.* Sections 4.1 and 5.2) and weak-to-moderate time clustering (see Sections 4.2 and 5.3), suggesting that the high residual stresses left by the absence of co-seismic release are driving the seismicity. Our study also revealed that strong seismicity started in the Lake Sapanca releasing step-over, located in between the Izmit-Sapanca and the Sapanca-Akyazi segments.

We detected strongly time clustered and intense seismicity at the eastern side of Lake Sapanca (see Section 4.2 and Figure 9). This seismicity takes place in a narrow depth interval at the bottom of the seismogenic zone ($\approx$ 10-13 km depth, *cf.* Figure 5C), suggesting that slip occurs in a mixed seismic and aseismic fashion and thus produce time clustered earthquake sequences (see Section 5.3, Dublanchet et al., 2013). The high b-value ($b \approx 1.2$) of the seismicity also points to low stress-drop events occurring in a low stress environment, typically featuring aseismic slip (*e.g.* Amelung & King, 1997).

Unlike its eastern counterpart, the seismicity at the western side of Lake Sapanca is shallow ($\approx$ 4-6 km, see Figure 5C) and weakly time clustered (Figure 9). Since previous studies have identified shallow creep along the Izmit-Sapanca segment (Çakir et al., 2012; Hussain et al., 2016; Aslan et al., 2019), updip aseismic slip is a possible driving mechanism of this seismicity. Such east-west differences over a short distance also likely reflect the heterogeneous geology of the region (*e.g.* Akbayram et al., 2013). Faults at the eastern side possibly intersect the so-called Sapanca complex at depth. This unit features weak and strong materials that could host slip with the above mentioned properties.

The complex interplay between the different structures of the North Anatolian Fault appears in stark contrast to the relatively simple co-seismic dynamics of the Izmit earthquake (*i.e.* rupture on almost straight and vertical fault segments Barka, 1999; Langridge et al., 2002). The results of our study emphasize the important role of secondary structures in the postseismic stage of the NAF, and possibly through the interseismic phase. We found that the Lake Sapanca step-over, and perhaps the step-over in the eastern Marmara Sea (*cf.* discussion in Section 5.4), was among the most active structures of the NAF and could be producing a significant extension in response to the co- and post-seismic displacement on the main fault segments. This interpretation is consistent with geodetic observations (Ergintav et al., 2009; Hearn et al., 2009) and points to the importance of modeling extension in the step-overs in order to understand stress accumulation along the NAF better.

7 Data and Resources

The earthquake catalog is available at the Zenodo data set repository (DOI: `10.5281/zenodo.6362973`). Our earthquake detection and location codes are available at the BPMF Python package repository `https://github.com/ebeauce/Seismic_BPMF` (version 1.0.1, last accessed December 2021).

The topographic data used for the maps were taken from the Shuttle Radar Topographic Mission (SRTM) 90-m database (`https://cgiarcsi.community/data/srtm-90m-digital-elevation-database-v4-1/`, last accessed December 2021). The maps were made with the Cartopy Python library (version 0.18.0, last accessed December 2021, Met Office, 2010 - 2015). The seismic data were recorded by the temporary array DANA (DANA , 2012, DOI: `https://doi.org/10.7914/SN/YH_2012`) and by the permanent KOERI stations (Kandilli Observatory And Earthquake Research Institute, Boğaziçi University, 1971, DOI: `https://doi.org/10.7914/SN/KO`).

Acknowledgements

This project has received funding from the European Research Council (ERC) under the European Union's Horizon H2020 research and innovation program (grant agreement No 742335). E.B. was also supported by funds associated with Robert D. van der Hilst's Schlumberger chair.

References

Akbayram, K., Okay, A. I., & Satır, M. (2013). Early cretaceous closure of the intra-pontide ocean in western pontides (northwestern turkey). *Journal of Geodynamics*, *65*, 38–55.

Aki, K. (1965). Maximum likelihood estimate of b in the formula log n= a-bm and its confidence limits. *Bull. Earthq. Res. Inst., Tokyo Univ.*, *43*, 237–239.

Amelung, F., & King, G. (1997). Earthquake scaling laws for creeping and non-creeping faults. *Geophysical research letters*, *24*(5), 507–510.

Amitrano, D. (2003). Brittle-ductile transition and associated seismicity: Experimental and numerical studies and relationship with the b value. *Journal of Geophysical Research: Solid Earth*, *108*(B1).

Aslan, G., Lasserre, C., Cakir, Z., Ergintav, S., Özarpaci, S., Dogan, U., … Renard, F. (2019). Shallow creep along the 1999 Izmit earthquake rupture (Turkey) from GPS and high temporal resolution interferometric synthetic aperture radar data (2011–2017). *Journal of Geophysical Research: Solid Earth*, *124*(2), 2218–2236.

Barka, A. (1999). The 17 august 1999 izmit earthquake. *Science*, *285*(5435), 1858–1859.

Barka, A., Akyuz, H., Altunel, E., Sunal, G., Cakir, Z., Dikbas, A., … others (2002). The surface rupture and slip distribution of the 17 august 1999 Izmit earthquake (m 7.4), North Anatolian fault. *Bulletin of the Seismological Society of America*, *92*(1), 43–60.

Bayrak, Y., & Öztürk, S. (2004). Spatial and temporal variations of the aftershock sequences of the 1999 izmit and düzce earthquakes. *Earth, planets and space*, *56*(10), 933–944.

Beaucé, E., Frank, W. B., Paul, A., Campillo, M., & van der Hilst, R. D. (2019). Systematic detection of clustered seismicity beneath the Southwestern Alps. *Journal of Geophysical Research: Solid Earth*, *124*(11), 11531–11548.

Beaucé, E., Frank, W. B., & Romanenko, A. (2018). Fast matched filter (FMF): An efficient seismic matched-filter search for both CPU and GPU architectures. *Seismological Research Letters*, *89*(1), 165–172.

Ben-Zion, Y., & Zaliapin, I. (2020). Localization and coalescence of seismicity before large earthquakes. *Geophysical Journal International*, *223*(1), 561–583.

Bohnhoff, M., Bulut, F., Görgün, E., Milkereit, C., & Dresen, G. (2008). Seismotectonic setting at the north anatolian fault zone after the 1999 mw= 7.4 izmit earthquake based on high-resolution aftershock locations. *Advances in Geosciences*, *14*, 85–92.

Bohnhoff, M., Grosser, H., & Dresen, G. (2006). Strain partitioning and stress rotation at the North Anatolian fault zone from aftershock focal mechanisms of the 1999 Izmit m w= 7.4 earthquake. *Geophysical Journal International*, *166*(1), 373–385.

Bohnhoff, M., Ickrath, M., & Dresen, G. (2016). Seismicity distribution in conjunction with spatiotemporal variations of coseismic slip and postseismic creep along the combined 1999 izmit-düzce rupture. *Tectonophysics*, *686*, 132–145.

Bouchon, M., Bouin, M.-P., Karabulut, H., Toksöz, M. N., Dietrich, M., & Rosakis, A. J. (2001). How fast is rupture during an earthquake? new insights from the 1999 Turkey earthquakes. *Geophysical Research Letters*, *28*(14), 2723–2726.

Bouchon, M., Karabulut, H., Aktar, M., Özalaybey, S., Schmittbuhl, J., & Bouin, M.-P. (2011). Extended nucleation of the 1999 mw 7.6 Izmit earthquake. *science*, *331*(6019), 877–880.

Bulut, F., Bohnhoff, M., Aktar, M., & Dresen, G. (2007). Characterization of aftershock-fault plane orientations of the 1999 izmit (turkey) earthquake using high-resolution aftershock locations. *Geophysical Research Letters*, *34*(20).

Bürgmann, R. (2018). The geophysics, geology and mechanics of slow fault slip. *Earth and Planetary Science Letters*, *495*, 112–134.

Bürgmann, R., Ergintav, S., Segall, P., Hearn, E. H., McClusky, S., Reilinger, R. E., … Zschau, J. (2002). Time-dependent distributed afterslip on and deep below the izmit earthquake rupture. *Bulletin of the Seismological Society of America*, *92*(1), 126–137.

Burridge, R., & Knopoff, L. (1967). Model and theoretical seismicity. *Bulletin of the seismological society of america*, *57*(3), 341–371.

Cakir, Z., Chabalier, J.-B. d., Armijo, R., Meyer, B., Barka, A., & Peltzer, G. (2003). Coseismic and early post-seismic slip associated with the 1999 izmit earthquake (turkey), from sar interferometry and tectonic field observations. *Geophysical Journal International*, *155*(1), 93–110.

Çakir, Z., Ergintav, S., Özener, H., Dogan, U., Akoglu, A. M., Meghraoui, M., & Reilinger, R. (2012). Onset of aseismic creep on major strike-slip faults. *Geology*, *40*(12), 1115–1118.

Cattania, C. (2019). Complex earthquake sequences on simple faults. *Geophysical Research Letters*, *46*(17-18), 10384–10393.

Cattania, C., & Segall, P. (2021). Precursory slow slip and foreshocks on rough faults. *Journal of Geophysical Research: Solid Earth*, *126*(4), e2020JB020430.

Crampin, S., Evans, R., & Üçer, S. B. (1985). Analysis of records of local earthquakes: the turkish dilatancy projects (tdp1 and tdp2). *Geophysical Journal International*, *83*(1), 1–16.

DANA . (2012). *Dense array for north anatolia.* International Federation of Digital Seismograph Networks. Retrieved from `http://www.fdsn.org/doi/10.7914/SN/YH_2012` doi: 10.7914/SN/YH_2012

Dublanchet, P. (2019). Scaling and variability of interacting repeating earthquake sequences controlled by asperity density. *Geophysical Research Letters*, *46*(21), 11950–11958.

Dublanchet, P., Bernard, P., & Favreau, P. (2013). Interactions and triggering in a 3-d rate-and-state asperity model. *Journal of Geophysical Research: Solid Earth*, *118*(5), 2225–2245.

Ergintav, S., McClusky, S., Hearn, E., Reilinger, R., Cakmak, R., Herring, T., … Tari, E. (2009). Seven years of postseismic deformation following the 1999, m= 7.4 and m= 7.2, izmit-düzce, turkey earthquake sequence. *Journal of Geophysical Research: Solid Earth*, *114*(B7).

Fan, W., & Shearer, P. M. (2016). Local near instantaneously dynamically triggered aftershocks of large earthquakes. *Science*, *353*(6304), 1133–1136.

Fischer, T., & Hainzl, S. (2021). The growth of earthquake clusters. *Frontiers in Earth Science*, *9*, 79.

Frank, W., & Shapiro, N. (2014). Automatic detection of low-frequency earthquakes (lfes) based on a beamformed network response. *Geophysical Journal International*, *197*(2), 1215–1223.

Frank, W. B., Shapiro, N. M., Husker, A. L., Kostoglodov, V., Gusev, A. A., & Campillo, M. (2016). The evolving interaction of low-frequency earthquakes during transient slip. *Science advances*, *2*(4), e1501616.

Gardner, J., & Knopoff, L. (1974). Is the sequence of earthquakes in Southern California, with aftershocks removed, Poissonian? *Bulletin of the Seismological Society of America*, *64*(5), 1363–1367.

Gibbons, S. J., & Ringdal, F. (2006). The detection of low magnitude seismic events using array-based waveform correlation. *Geophysical Journal International*, *165*(1), 149–166.

Gomberg, J., Beeler, N., Blanpied, M., & Bodin, P. (1998). Earthquake triggering by transient and static deformations. *Journal of Geophysical Research: Solid Earth*, *103*(B10), 24411–24426.

Gulia, L., & Wiemer, S. (2019). Real-time discrimination of earthquake foreshocks and aftershocks. *Nature*, *574*(7777), 193–199.

Gutenberg, B., & Richter, C. (1941). *Seismicity of the earth* (Vol. 34). Geological Society of America.

Hainzl, S., Scherbaum, F., & Beauval, C. (2006). Estimating background activity based on interevent-time distribution. *Bulletin of the Seismological Society of America*, *96*(1), 313–320.

Harris, R. A., Simpson, R. W., & Reasenberg, P. A. (1995). Influence of static stress changes on earthquake locations in southern california. *Nature*, *375*(6528), 221–224.

Hearn, E., McClusky, S., Ergintav, S., & Reilinger, R. (2009). Izmit earthquake postseismic deformation and dynamics of the north anatolian fault zone. *Journal of Geophysical Research: Solid Earth*, *114*(B8).

Honda, R., & Aoi, S. (2009). Array back-projection imaging of the 2007 Niigataken Chuetsu-oki earthquake striking the world's largest nuclear power plant. *Bulletin of the Seismological Society of America*, *99*(1), 141–147.

Hussain, E., Wright, T. J., Walters, R. J., Bekaert, D., Hooper, A., & Houseman, G. A. (2016). Geodetic observations of postseismic creep in the decade after the 1999 Izmit earthquake, Turkey: Implications for a shallow slip deficit. *Journal of Geophysical Research: Solid Earth*, *121*(4), 2980–3001.

Ickrath, M., Bohnhoff, M., Dresen, G., Martinez-Garzon, P., Bulut, F., Kwiatek, G., & Germer, O. (2015). Detailed analysis of spatiotemporal variations of the stress field orientation along the izmit-düzce rupture in nw turkey from inversion of first-motion polarity data. *Geophysical Journal International*, *202*(3), 2120–2132.

Ishii, M., Shearer, P. M., Houston, H., & Vidale, J. E. (2005). Extent, duration and speed of the 2004 Sumatra–Andaman earthquake imaged by the Hi-Net array. *Nature*, *435*(7044), 933.

Kahraman, M., Cornwell, D. G., Thompson, D. A., Rost, S., Houseman, G. A., Türkelli, N., … Gülen, L. (2015, Nov). Crustal-scale shear zones and heterogeneous structure beneath the North Anatolian Fault Zone, Turkey, revealed by a high-density seismometer array. *Earth Planet. Sci. Lett.*, *430*, 129–139. doi: 10.1016/j.epsl.2015.08.014

Kandilli Observatory And Earthquake Research Institute, Boğaziçi University. (1971). *Bogazici university kandilli observatory and earthquake research institute.* International Federation of Digital Seismograph Networks. Retrieved from `http://www.fdsn.org/doi/10.7914/SN/KO` doi: 10.7914/SN/KO

Karabulut, H., Schmittbuhl, J., Özalaybey, S., Lengline, O., Kömeç-Mutlu, A., Durand, V., … Bouin, M. (2011). Evolution of the seismicity in the eastern Marmara Sea a decade before and after the 17 August 1999 Izmit earthquake. *Tectonophysics*, *510*(1-2), 17–27.

Karahan, A. E., Berckhemer, H., & Baier, B. (2001). Crustal structure at the western end of the North Anatolian Fault Zone from deep seismic sounding.

King, G., & Cocco, M. (2001). Fault interaction by elastic stress changes: New clues from earthquake sequences. In *Advances in geophysics* (Vol. 44, pp. 1–VIII). Elsevier.

Langridge, R., Stenner, H. D., Fumal, T., Christofferson, S., Rockwell, T., Hartleb, R., … Barka, A. (2002). Geometry, slip distribution, and kinematics of surface rupture on the sakarya fault segment during the 17 august 1999 izmit, turkey, earthquake. *Bulletin of the Seismological Society of America*, *92*(1), 107–125.

Lee, H.-K., & Schwarcz, H. P. (1995). Fractal clustering of fault activity in california. *Geology*, *23*(4), 377–380.

Le Pichon, X., & Angelier, J. (1979). The hellenic arc and trench system: a key to the neotectonic evolution of the eastern mediterranean area. *Tectonophysics*, *60*(1-2), 1–42.

Lohman, R., & McGuire, J. (2007). Earthquake swarms driven by aseismic creep in the salton trough, california. *Journal of Geophysical Research: Solid Earth*,

112(B4).
Lomax, A., Michelini, A., Curtis, A., & Meyers, R. (2009). Earthquake location, direct, global-search methods. *Encyclopedia of complexity and systems science*, *5*, 2449–2473.
Lomax, A., Virieux, J., Volant, P., & Berge-Thierry, C. (2000). Probabilistic earthquake location in 3D and layered models. In *Advances in seismic event location* (pp. 101–134). Springer.
Lovell, J., Crampin, S., Evans, R., & Üçer, S. B. (1987). Microearthquakes in the tdp swarm, turkey: clustering in space and time. *Geophysical Journal International*, *91*(2), 313–330.
Lowen, S. B., & Teich, M. C. (2005). *Fractal-based point processes* (Vol. 366). John Wiley & Sons.
Marsan, D., & Lengline, O. (2008). Extending earthquakes' reach through cascading. *Science*, *319*(5866), 1076–1079.
McClusky, S., Balassanian, S., Barka, A., Demir, C., Ergintav, S., Georgiev, I., ... others (2000). Global positioning system constraints on plate kinematics and dynamics in the eastern mediterranean and caucasus. *Journal of Geophysical Research: Solid Earth*, *105*(B3), 5695–5719.
Meade, B. J., Hager, B. H., McClusky, S. C., Reilinger, R. E., Ergintav, S., Lenk, O., ... Ozener, H. (2002). Estimates of seismic potential in the marmara sea region from block models of secular deformation constrained by global positioning system measurements. *Bulletin of the Seismological Society of America*, *92*(1), 208–215.
Met Office. (2010 - 2015). Cartopy: a cartographic python library with a matplotlib interface [Computer software manual]. Exeter, Devon. Retrieved from `http://scitools.org.uk/cartopy`
Mogi, K. (1962). Study of elastic shocks caused by the fracture of heterogeneous materials and its geophysics. *Rev. Geophys*, *15*, 77–104.
Moreau, L., Stehly, L., Boué, P., Lu, Y., Larose, E., & Campillo, M. (2017). Improving ambient noise correlation functions with an SVD-based Wiener filter. *Geophysical Journal International*, *211*(1), 418–426.
Mori, J., & Abercrombie, R. E. (1997). Depth dependence of earthquake frequency-magnitude distributions in california: Implications for rupture initiation. *Journal of Geophysical Research: Solid Earth*, *102*(B7), 15081–15090.
Ozalaybey, S., Ergin, M., Aktar, M., Tapirdamaz, C., Biçmen, F., & Yörük, A. (2002). The 1999 izmit earthquake sequence in turkey: seismological and tectonic aspects. *Bulletin of the Seismological Society of America*, *92*(1), 376–386.
Papaleo, E., Cornwell, D., & Rawlinson, N. (2018). Constraints on North Anatolian Fault Zone width in the crust and upper mantle from S wave teleseismic tomography. *Journal of Geophysical Research: Solid Earth*, *123*(4), 2908–2922.
Parsons, T., Toda, S., Stein, R. S., Barka, A., & Dieterich, J. H. (2000). Heightened odds of large earthquakes near istanbul: An interaction-based probability calculation. *Science*, *288*(5466), 661–665.
Perfettini, H., & Avouac, J.-P. (2004). Postseismic relaxation driven by brittle creep: A possible mechanism to reconcile geodetic measurements and the decay rate of aftershocks, application to the chi-chi earthquake, taiwan. *Journal of Geophysical Research: Solid Earth*, *109*(B2).
Pınar, A., Üçer, S., Honkura, Y., Sezgin, N., Ito, A., Barış, Ş., ... Horiuchi, S. (2010). Spatial variation of the stress field along the fault rupture zone of the 1999 Izmit earthquake. *Earth, planets and space*, *62*(3), 237–256.
Poupinet, G., Ellsworth, W., & Frechet, J. (1984). Monitoring velocity variations in the crust using earthquake doublets: An application to the calaveras fault, california. *Journal of Geophysical Research: Solid Earth*, *89*(B7), 5719–5731.
Poyraz, S. A., Teoman, M. U., Türkelli, N., Kahraman, M., Cambaz, D., Mutlu, A.,

... others (2015). New constraints on micro-seismicity and stress state in the western part of the North Anatolian Fault Zone: Observations from a dense seismic array. *Tectonophysics*, *656*, 190–201.

Reilinger, R., Ergintav, S., Bürgmann, R., McClusky, S., Lenk, O., Barka, A., ... others (2000). Coseismic and postseismic fault slip for the 17 august 1999, m= 7.5, izmit, turkey earthquake. *Science*, *289*(5484), 1519–1524.

Reilinger, R., McClusky, S., Vernant, P., Lawrence, S., Ergintav, S., Cakmak, R., ... others (2006). GPS constraints on continental deformation in the Africa-Arabia-Eurasia continental collision zone and implications for the dynamics of plate interactions. *Journal of Geophysical Research: Solid Earth*, *111*(B5).

Ross, Z. E., Trugman, D. T., Hauksson, E., & Shearer, P. M. (2019). Searching for hidden earthquakes in Southern California. *Science*, eaaw6888.

Scholz, C. H. (1968). The frequency-magnitude relation of microfracturing in rock and its relation to earthquakes. *Bulletin of the seismological society of America*, *58*(1), 399–415.

Scholz, C. H. (1998). Earthquakes and friction laws. *Nature*, *391*(6662), 37–42.

Scholz, C. H. (2015). On the stress dependence of the earthquake b value. *Geophysical Research Letters*, *42*(5), 1399–1402.

Shelly, D. R., Beroza, G. C., & Ide, S. (2007). Non-volcanic tremor and low-frequency earthquake swarms. *Nature*, *446*(7133), 305.

Smalley Jr, R. F., Chatelain, J.-L., Turcotte, D. L., & Prévot, R. (1987). A fractal approach to the clustering of earthquakes: applications to the seismicity of the new hebrides. *Bulletin of the Seismological Society of America*, *77*(4), 1368–1381.

Stein, R. S., Barka, A. A., & Dieterich, J. H. (1997). Progressive failure on the North Anatolian fault since 1939 by earthquake stress triggering. *Geophysical Journal International*, *128*(3), 594–604.

Taylor, G., Rost, S., Houseman, G. A., & Hillers, G. (2019). Near-surface structure of the North Anatolian Fault zone from Rayleigh and Love wave tomography using ambient seismic noise. *Solid Earth*, *10*(2), 363–378.

Toksoz, M., Reilinger, R., Doll, C., Barka, A., & Yalcin, N. (1999). Izmit (Turkey) earthquake of 17 August 1999: first report. *Seismological Research Letters*, *70*(6), 669–679.

Toksöz, M., Shakal, A., & Michael, A. (1979). Space-time migration of earthquakes along the North Anatolian fault zone and seismic gaps. *Pure and Applied Geophysics*, *117*(6), 1258–1270.

Trugman, D. T., & Shearer, P. M. (2017). GrowClust: A hierarchical clustering algorithm for relative earthquake relocation, with application to the Spanish Springs and Sheldon, Nevada, earthquake sequences. *Seismological Research Letters*, *88*(2A), 379–391.

Utkucu, M., Nalbant, S. S., McCloskey, J., Steacy, S., & Alptekin, Ö. (2003). Slip distribution and stress changes associated with the 1999 november 12, düzce (turkey) earthquake (mw= 7.1). *Geophysical Journal International*, *153*(1), 229–241.

Waldhauser, F., & Ellsworth, W. L. (2000). A double-difference earthquake location algorithm: Method and application to the northern hayward fault, california. *Bulletin of the Seismological Society of America*, *90*(6), 1353–1368.

Walker, K. T., Ishii, M., & Shearer, P. M. (2005). Rupture details of the 28 March 2005 Sumatra Mw 8.6 earthquake imaged with teleseismic P waves. *Geophysical Research Letters*, *32*(24).

White, M. C., Fang, H., Nakata, N., & Ben-Zion, Y. (2020). PyKonal: A Python Package for Solving the Eikonal Equation in Spherical and Cartesian Coordinates Using the Fast Marching Method. *Seismological Research Letters*, *91*(4), 2378–2389.

Wiemer, S., & Katsumata, K. (1999). Spatial variability of seismicity parameters in aftershock zones. *Journal of Geophysical Research: Solid Earth*, *104*(B6), 13135–13151.

Wiemer, S., & Wyss, M. (1997). Mapping the frequency-magnitude distribution in asperities: An improved technique to calculate recurrence times? *Journal of Geophysical Research: Solid Earth*, *102*(B7), 15115–15128.

Zhu, W., & Beroza, G. C. (2019). PhaseNet: a deep-neural-network-based seismic arrival-time picking method. *Geophysical Journal International*, *216*(1), 261–273.